

ADF22-WEB: ALMA and JWST (sub)kpc-scale views of dusty star-forming galaxies in a $z \approx 3$ proto-cluster

HIDEKI UMEHATA,^{1,2} MARIKO KUBO,³ IAN SMAIL,⁴ BRET D. LEHMER,⁵ ERIK B. MONSON,⁶ KOUICHIRO NAKANISHI,^{7,8} AND YUICHI MATSUDA^{7,8}

¹*Institute for Advanced Research, Nagoya University, Furocho, Chikusa, Nagoya 464-8602, Japan*

²*Department of Physics, Graduate School of Science, Nagoya University, Furocho, Chikusa, Nagoya 464-8602, Japan*

³*Astronomical Institute, Tohoku University, 6-3, Aramaki, Aoba, Sendai, Miyagi, 980-8578, Japan*

⁴*Centre for Extragalactic Astronomy, Department of Physics, Durham University, South Road, Durham DH1 3LE, UK*

⁵*Department of Physics, University of Arkansas, 226 Physics Building, 825 West Dickson Street, Fayetteville, AR 72701, USA*

⁶*Department of Astronomy and Astrophysics, The Pennsylvania State University, 525 Davey Lab, University Park, PA 16802, USA*

⁷*National Astronomical Observatory of Japan, 2-21-1 Osawa, Mitaka, Tokyo 181-8588, Japan*

⁸*Department of Astronomical Science, The Graduate University for Advanced Studies, SOKENDAI, 2-21-1 Osawa, Mitaka, Tokyo 181-8588, Japan*

ABSTRACT

We present a morphological analysis of ALMA and JWST NIRC*am* images of nine dusty star-forming galaxies (DSFGs) at $z_{\text{spec}} \approx 3.09$, all embedded within the cosmic web filaments at the SSA22 proto-cluster core. The ALMA 870 μm and 1.1 mm images are obtained at spatial resolutions ranging from 0.5'' to 0.05'' (350 pc at $z = 3.09$). The high-resolution images enable us to resolve inner structures traced by dust continuum, identifying compact dusty cores, clumps, and offset ridges within bars. Sérsic profile fit was performed for both ALMA 870 μm and NIRC*am* F444W images at comparable resolutions ($\sim 0.15''$). The Sérsic index measured for 870 μm , masking bright regions, indicates values close to unity, suggesting that dust emission arises from disks with superimposed compact core components. For the JWST F444W images (restframe $\sim 1 \mu\text{m}$), the Sérsic indices range between $n_{\text{F444W}} \sim 1 - 3$, pointing to the coexistence of bulges and stellar disks in these DSFGs. A comparison of dust mass surface density, n_{F444W} , and F200W–F444W color (restframe $\sim 0.5 - 1 \mu\text{m}$) reveals diversity among the DSFGs, likely reflecting different evolutionary stages including some DSFGs with red cores, indicating ongoing rapid bulge growth phases heavily obscured by dust. The predominantly disk-like morphologies observed in most DSFGs in the proto-cluster core contrast sharply with early-type morphologies that dominate the highest density environment in the local universe. This suggests that we are witnessing the early formation of the morphology-density relation, as massive galaxies undergo rapid growth as late-type galaxies fueled by cosmic web gas filaments.

Keywords: galaxies: evolution - galaxies: star formation

1. INTRODUCTION

The cold dark matter (CDM) model predicts that galaxy formation and evolution are tightly linked to the growth of large-scale cosmic structures, known as the cosmic web, which consists of interconnected dark matter and baryonic filaments shaping galaxy distribution (e.g., Bond et al. 1996; Lemson & Kauffmann 1999; Springel et al. 2005). Understanding the environments in which galaxies reside, including their positions within the cosmic web, is therefore essential for unraveling the processes driving galaxy formation and evolution across cosmic time.

In the local universe, dense environments such as galaxy clusters are predominantly populated by passive, early-type galaxies, whereas less dense regions are characterized by star-forming, late-type galaxies (e.g., Dressler 1980). Similarly, in the local-to-nearby universe, clusters exhibit a prominent red sequence of passive galaxies (e.g., Ellis et al. 1997; Kodama et al. 1998; 2007; Smith et al. 2012). The passive nature of these galaxies indicates that the majority of their stars formed at least $\sim 1 - 2$ Gyr prior to the epoch of observation. Cosmological simulations also predict that the progenitors of massive elliptical galaxies, which are in actively star-forming phases, are preferentially located in high-

density environments at $z \gtrsim 2 - 3$ (e.g. De Lucia et al. 2006).

Dusty star-forming galaxies (DSFGs), also known as submillimeter galaxies (SMGs), are characterized by their remarkable submillimeter flux resulting from intense, dust-obscured star formation (for reviews, see Blain et al. 2002; Casey et al. 2014; Hodge & da Cunha 2020). Since the discovery of DSFGs (Smail et al. 1997; Hughes et al. 1998; Barger et al. 1998; Ivison et al. 1998), their starburst nature in the early universe has led to suggestions that they are plausible progenitors of local elliptical galaxies (e.g., Eales et al. 1999; Toft et al. 2014). Testing this scenario requires uncovering the environments where DSFGs reside, characterizing the stellar assembly occurring within DSFGs, and connecting the formation and evolution of DSFGs to the larger structure formation processes.

Before the advent of the Atacama Large Millimeter/submillimeter Array (ALMA), substantial efforts were made to study DSFGs and their environments (e.g. Stevens et al. 2003; Blain et al. 2004; Greve et al. 2005; Daddi et al. 2009; Tamura et al. 2009; Walter et al. 2012; Umehata et al. 2014). A significant breakthrough came when Umehata et al. (2015) identified eight individual DSFGs with spectroscopically confirmed redshifts (z_{spec}) within a $z = 3.1$ proto-cluster core. This marked the first discovery of a large number of DSFGs associated with proto-clusters, free from source confusion at submillimeter and millimeter wavelengths. The advent of ALMA has since expanded our knowledge of DSFGs in proto-clusters, reaching redshifts as high as $z \gtrsim 5$ (e.g., Riechers et al. 2013; Oteo et al. 2018; Miller et al. 2018; Sun et al. 2024).

Despite significant advancements, one major obstacle in understanding the nature, origins, and evolution of DSFGs is the lack of spatial resolution. The heavy dust extinction in DSFGs obscures a substantial fraction of stellar emission in wavelengths accessible with the Hubble Space Telescope (HST) (e.g. Swinbank et al. 2010; Chen et al. 2015; Monson et al. 2021). Meanwhile, the limited spatial resolution of the Spitzer Space Telescope has made it challenging to study stellar structures in the rest frame near- to mid-infrared wavelengths, which are better suited for tracing stellar mass distributions (e.g. Hainline et al. 2011; Wardlow et al. 2011; Simpson et al. 2014; Umehata et al. 2014).

In terms of dust continuum observations, while ALMA has significantly improved the identification of individual DSFGs through snapshot surveys and deep mosaics (e.g. Hodge et al. 2013; Weiß et al. 2013; Ikarashi et al. 2015; Dunlop et al. 2017; Stach et al. 2019), achieving high spatial resolution data with high fidelity remains

a challenge even with ALMA. These limitations continue to hinder a comprehensive understanding of DSFGs, both in general fields and in biased environments, such as proto-clusters.

We are gradually overcoming these difficulties. For instance, high-resolution mapping of the dust continuum in DSFGs at sub-kpc scales has unveiled internal structures indicative of bars and spiral arms (e.g., Iono et al. 2016; Hodge et al. 2016; 2019; 2025; Tadaki et al. 2018; Gullberg et al. 2018). Furthermore, the James Webb Space Telescope (JWST) has dramatically improved our ability to resolve stellar structures. Since its launch, studies have investigated the stellar structures in DSFGs, with some reporting disc-like profiles indicative of secular evolutionary processes, while others reveal signatures of interactions (e.g., Chen et al. 2022; Cheng et al. 2023; Colina et al. 2023; Gillman et al. 2023; 2024; Hodge et al. 2025).

Despite these advances, critical challenges remain. First, it is necessary to construct samples observed with both ALMA and JWST at comparably high resolutions to enable a comprehensive interpretation of DSFGs (e.g. Hodge et al. 2025). Second, as noted earlier, it is fundamentally important to connect DSFGs to their underlying environments, requiring detailed studies in notable proto-clusters in the early universe.

Motivated by these challenges, we have initiated the “ADF22-WEB” project (Umehata et al. 2024). This is an extension of the ALMA Deep Field in SSA22 (ADF22) project, which has been developed since ALMA Cycle-2 (e.g., Umehata et al. 2015; 2017; 2018; 2020; Hayatsu et al. 2017). In the core region of the SSA22 proto-cluster at $z = 3.1$ (Steidel et al. 1998; Hayashino et al. 2004; Matsuda et al. 2005), about twenty DSFGs and eight X-ray AGNs, including six DSFGs hosting X-ray AGNs, are embedded in Ly α filaments stretching over 4 comoving Mpc (Umehata et al. 2019; S. Huang et al., in preparation). This field provides an invaluable laboratory for investigating and uncovering how galaxies form and evolve along cosmic web filaments.

In this paper, we present new ALMA and JWST observation of nine DSFGs at $z_{\text{spec}} = 3.09$ in the ADF22 field and discuss their nature based on resolved views of stellar and dust structures. The structure of this paper is as follows. In §2, we describe the observations with ALMA and JWST. In §3, we present a detailed morphological analysis of the ALMA continuum images. In §4, we present the JWST/NIRCam images and compare them with the ALMA images. In §5, we discuss the origins of the dust emission, bulge formation, morphological transformation, and the influ-

ence of the cosmic web on galaxy evolution. We conclude in §6. We adopt a standard concordance cosmology with $H_0 = 70 \text{ km s}^{-1} \text{ Mpc}^{-1}$, $\Omega_m = 0.30$, and $\Omega_\Lambda = 0.70$. Here, H_0 is the Hubble constant, and Ω_m and Ω_Λ are the matter density and dark energy density at the present time, respectively. This cosmology gives a scale of $7.63 \text{ kpc per arcsec}$ at $z = 3.09$.

2. OBSERVATION AND DATA REDUCTION

2.1. Target Selection

Among the 16 DSFGs at $z_{\text{spec}} \approx 3.09$ in ADF22 reported in Umehata et al. (2019) (see also Umehata et al. 2015; 2017), we selected the brightest six DSFGs (ADF22.A1, A3, A4, A5, A6, and A7) as primary targets. They are ULIRG-class DSFGs (IR luminosity $L_{\text{IR}} \gtrsim 10^{12} L_\odot$, Umehata et al. 2017) and suitable to investigate the nature of such *classical*, relatively bright DSFGs. Four of them have been known to harbor X-ray AGNs (Tamura et al. 2010; Umehata et al. 2015; 2019; Monson et al. 2023). We also discuss three additional DSFGs (ADF22.A10, A11, and A16) as secondary targets. These DSFGs are located in the vicinity of the primary target ADF22.A4 and were simultaneously observed and detected by both ALMA and JWST, while the fidelity of the dust continuum emission is reduced slightly due to their relatively submm-faint nature.

2.2. ALMA Observation

2.2.1. Band-6 observations

Observations in ALMA Band-6 to map the 1.1 mm dust continuum were conducted in August 2021 as a Cycle-7 program (PI Umehata, 2019.1.00008.S). The data were taken in four execution blocks (EBs). For all, the array was configured in C43-8 with 43–49 antennas, which offered baseline lengths of 46 m to 12600 m. The precipitable water vapor (PWV) $\sim 0.5 \text{ mm}$ is suitable for Band-6 observations. The six primary target fields were observed and a total on-source time for each source was 31.4 min. J2253+1608 was used as a band-pass and flux calibrator, while J2226+0052 was regularly checked for phase calibration. The four spectral windows were centered at frequencies of 253.0, 254.8, 267.0, and 269.0 GHz. The set-up encompasses CO(9–8) and OH $^+(1_1 \rightarrow 0_1)$ lines. We masked the lines if they are detected. Data reduction was carried out using version 6.1.0 and 6.5.0 of the CASA package. The continuum image was generated from line-free channels using the TCLEAN task. The representative frequency is 261.51 GHz (or 1.146 mm). We create a mosaic by combining two nearby fields, ADF22.A1 and ADF22.A7,

to enhance sensitivity. We employ the `usemask` parameter set to `auto-multithresh`. In the initial pass of mask creation for each channel, only pixels with a signal-to-noise ratio (S/N) of 4.5 or higher are included (`noisethreshold = 4.5`). Subsequently, the mask is expanded to encompass regions with lower S/N values (`lownoisethreshold = 1.5`). The regions identified through automasking are then cleaned down to the 2σ level (`nsigma = 2` in TCLEAN). Images at two different spatial resolutions were obtained to track dust continuum emission at a different spatial scale. Using the Briggs weighting with the robust parameter 1.0, images have angular resolution of $0.05''$. Applying natural weighting with UVTAPER set to $0.038''$ produced a synthesized beam size of $0.08''$. We summarize the beam size and rms noise level in Table 1.

2.2.2. Band-7 observations

ALMA Band-7 observations for the six fields centered on the brightest DSFGs were performed as a Cycle-8 project (PI Umehata, 2021.1.00071.S). The C43-3 and C43-6 array configurations were utilized in May and July in 2022. The combination of array configurations are designed to be sensitive to emission on various scales. Data were obtained through two EBs in C43-3 and three EBs in C43-6, yielding on-source time per field of 8 min and 21 min, respectively. The covered base line lengths by the two array configurations ranges from 15 m to 2617 m, and 42–27 12-m antennas were used. PWV was $\sim 0.5 \text{ mm}$. The correlator was set up with two spectral windows of 1.875 GHz bandwidth (dual polarization) each per sideband. The spectral windows had central frequencies of 336.5, 338.4, 348.5, and 350.5 GHz, respectively. The representative frequency is 343.47 GHz, which corresponds to $\approx 870 \mu\text{m}$ at the observed frame. Data reduction was performed using version CASA 6.5.0, mapped with the TCLEAN task as in the case of Band-6 data. Similarly we combined the ADF22.A1 and ADF22.A7 fields to obtain a single image. We make two-types of images. First we adopted the Briggs weighting with the robust parameter 0.5, which resulted in $\sim 0.15''$ resolution. Second we imaged only with the C43-3 array data with natural weighting to investigate the flux distribution in a way which is not well resolved. These maps have $\sim 0.5''$ resolutions. Observational parameters are summarized in Table 1.

2.3. JWST Observation

The ADF22 field was observed with JWST/NIRCam as part of the JWST Cycle-2 program (PI Umehata, GO 3547) as reported in Umehata et al. (2024). Here we briefly describe the observation. Images are obtained with four filters; F115W, F200W, F356W, and F444W.

Table 1. ALMA band 6 and 7 observation parameters

ALMA Band	Wavelength	Beam size	rms Noise	Beam size	rms Noise
			($\mu\text{Jy beam}^{-1}$)		($\mu\text{Jy beam}^{-1}$)
Band-6	1.1 mm	$0.047'' \times 0.039''$	17	$0.079'' \times 0.072''$	19
Band-7	870 μm	$0.15'' \times 0.14''$	28 (24)	$0.54'' \times 0.48''$	53 (47)

NOTE—A mosaic image was created by combining the two fields, ADF22.A1 and ADF22.A7, resulting in a slightly improved noise level for the two DSFGs in Band-7 (as indicated in the brackets). The RMS noise levels at the source positions were measured after applying the primary beam correction.

Each filter had an exposure time of 1869 sec using the STANDARD subpixel dither pattern without primary dithering. The observations employed the MEDIUM8 readout mode. Data reduction followed the JWST calibration pipeline (v.1.8.4) with additional steps for “snowball” removal, wisp subtraction, and 1/f noise correction, based on CEERS team guidelines (Bagley et al. 2023). The 5σ limiting magnitudes for a $0.2''$ diameter aperture are 29.74, 29.01, 29.15, 29.49, 29.00 AB mag for F115W, F200W, F356W, and F444W, respectively, with the PSF of each image matched to F444W. To register coordinates accurately and perform fair comparison between JWST and ALMA images, we first match the xy coordinates among the four-band NIRCcam images to each other, and reconfigure the wcs based on the Gaia DR3 stars’ coordinates. We then refined the alignment by minimizing systematic offsets between the emission peaks in the ALMA 870 μm and NIRCcam F444W images, assuming that there is no systematic offset between the two (though each peak does not necessarily match perfectly). This approach, utilizing the advantages of multiple detections in the same field (i.e., ADF22), ensures consistency of astrometry between ALMA and NIRCcam images within the native pixel scale of the F444W image ($0.063'' \text{ pix}^{-1}$).

3. MEASUREMENTS ON DUST CONTINUUM

3.1. Overview and flux measurements

Fig. 1 presents ALMA dust continuum maps of the six bright DSFGs at $z = 3.09$, shown at various spatial resolutions and scales. Each resolution offers unique advantages. The 870 μm maps, obtained at resolutions of $0.5''$ (3.8 kpc at $z = 3.09$) and $0.15''$ (1.1 kpc at $z = 3.09$), provide both (nearly) unresolved and resolved views of the galaxies on a whole galaxy scale with high significance. In contrast, the 1.1 mm maps, with resolutions of $0.08''$ (600 pc at $z = 3.09$) and $0.05''$ (350 pc at $z = 3.09$), reveal detailed inner structures, though they less sensitive for tracing the total emission of the

galaxies with high fidelity. These high-resolution maps uncovered complex inner structures of the dust continuum emission within the proto-cluster DSFGs (Fig. 1.)

A first step we carried out was to measure flux densities of the DSFGs in these maps. We use the 870 μm images at $0.5''$ to estimate the total flux at the wavelength. We found that a Gaussian fit using CASA/IMFIT often leaves significant residuals (both positive and negative), suggesting that the use of a single Gaussian does not work to describe observed surface brightness profiles even at the 3.8 kpc resolution. Here we measure fluxes, counting emissions enclosed by 2σ contours (To measure profiles more accurately, we will perform a more detailed profile fit in §3.3). These measurements are generally consistent with those of CASA/IMFIT ($\langle S_{\text{Imfit}}/S_{\text{ctr}} \rangle = 1.03 \pm 0.07$). The ratio is calculated as the weighted average of the individual measurement ratios and the error is determined using the standard error of the weighted average. Considering the complex morphologies in finer resolution maps, we generally adopt this method and measure fluxes enclosed within 2σ contours for each map. These measurements were summarized in Table 2. Peak fluxes in the 1.1mm images at $0.05''$ were also listed. We also added the 1.1 mm total fluxes at $1.0''$ resolution measured with the CASA/IMFIT (The image were obtained using independent Band-6 observations with the modest angular resolution. Details will be presented in S. Huang et al. in preparation).

3.2. Recovered flux ratios

The 870 μm flux measured at $0.15''$ resolution and the 1.1 mm flux at $0.08''$ resolution account for approximately 90% – 110% of the total fluxes measured at $0.5''$ – $1.0''$ for bright DSFGs (Table 2). In the case of the $0.08''$ resolution 1.1 mm images, the maximum recoverable scale is ≈ 0.5 – $0.6''$ and the spatial resolution corresponds to scales of 600 pc at $z = 3.1$. The high fraction of recovery fluxes suggests that the majority of the flux is recovered at these scales. On the other hand, the diversity of flux recovery rates becomes more appar-

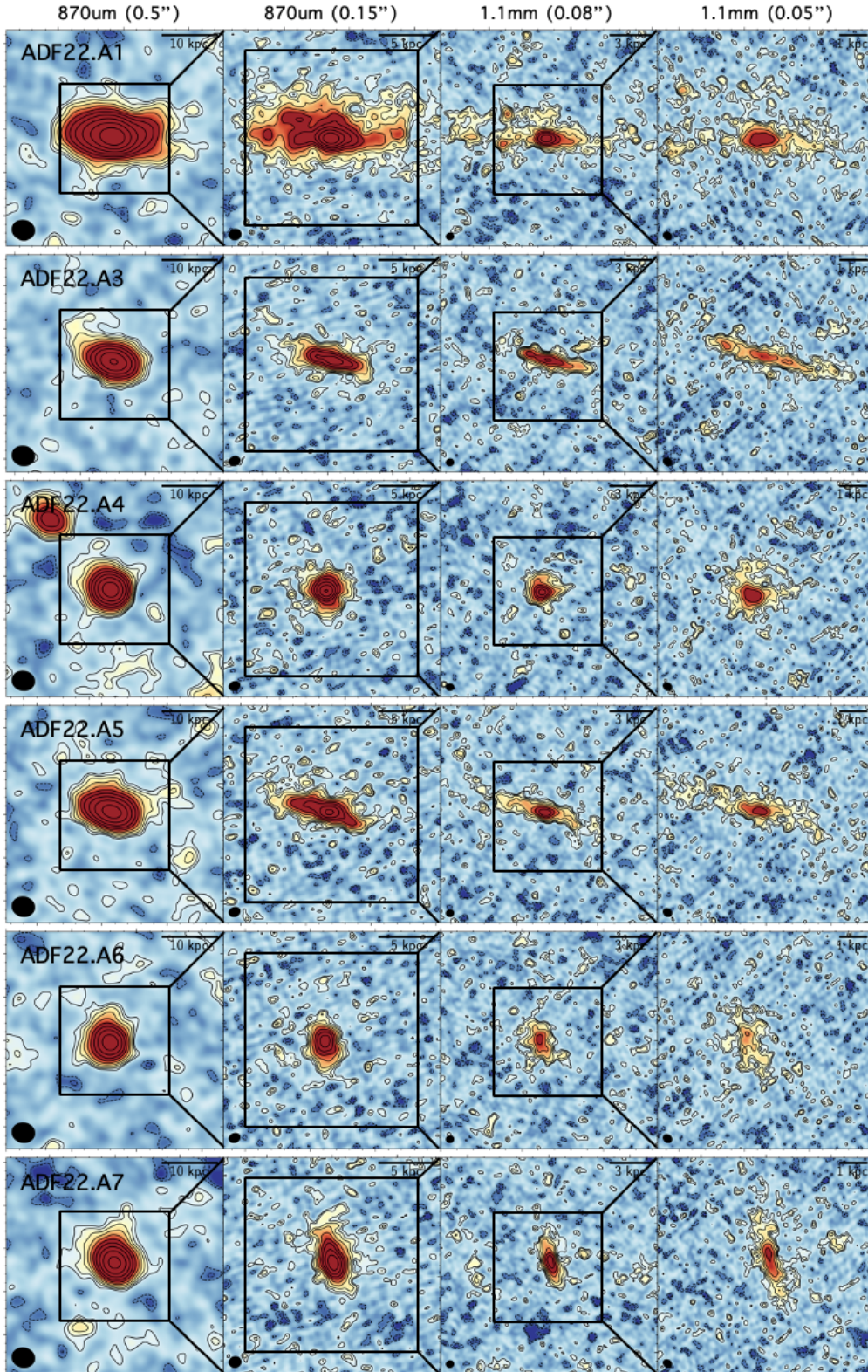


Figure 1. The cutout images of the six brightest $z = 3.09$ DSGs in ADF22. From left to right, close-up views are shown, with each inserted square indicating the area highlighted in the adjacent tile. Each map presents $870\ \mu\text{m}$ images with resolutions of $0.5''$ and $0.15''$, as well as 1.1mm images with resolutions of $0.08''$ and $0.05''$, respectively. The panel sizes are $5'' \times 5''$, $2.5'' \times 2.5''$, $2'' \times 2''$, and $1'' \times 1''$, respectively. Contours correspond to $\pm\sigma \times 1.5^n$, with $n = 1$ to $n = 11$. The dust emission is resolved down to $0.05''$ (350 pc at $z = 3.09$), revealing substructures that suggest bright central cores and offset ridges in bars. We discuss the origins of the dust emission in §5.1.

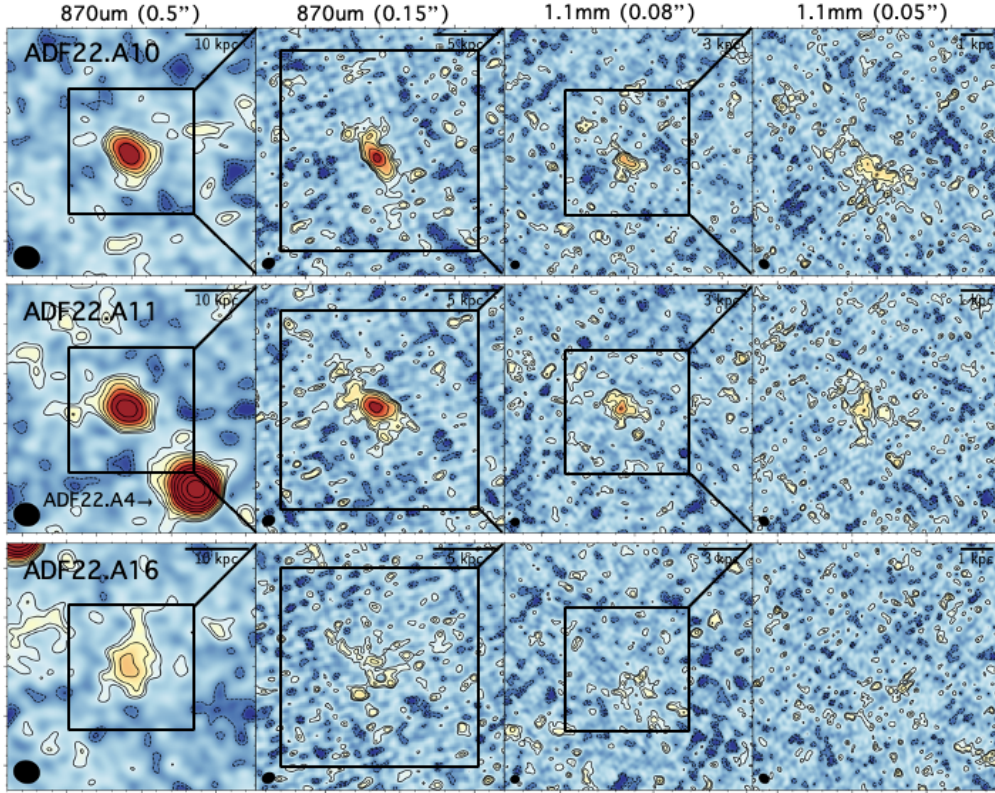


Figure 2. The cutout images of three $z = 3.09$ DSGs in the vicinity of ADF22.A4. Panels are as shown in Fig. 1.

Table 2. ALMA Flux measurements

ID	R.A.	Dec.	$S_{870\mu\text{m},0.5''}$	$S_{870\mu\text{m},0.15''}$	$S_{1.1\text{mm},1.0''}$	$S_{1.1\text{mm},0.08''}$	$S_{1.1\text{mm},0.05''}$	$S_{1.1\text{mm},0.05''}^{\text{peak}}$
	IRCS	IRCS	(mJy)	(mJy)	(mJy)	(mJy)	(mJy)	(mJy)
ADF22.A1	22:17:32.42	00:17:43.86	14.67 ± 0.18	14.40 ± 0.19	6.15 ± 0.06	5.86 ± 0.15	3.71 ± 0.11	0.26 ± 0.02
ADF22.A3	22:17:35.15	00:15:37.24	5.09 ± 0.14	4.75 ± 0.13	2.23 ± 0.04	2.28 ± 0.08	2.18 ± 0.09	0.19 ± 0.02
ADF22.A4	22:17:36.97	00:18:20.68	5.23 ± 0.13	4.98 ± 0.12	2.26 ± 0.09	2.20 ± 0.08	2.11 ± 0.09	0.28 ± 0.02
ADF22.A5	22:17:31.49	00:17:58.08	6.67 ± 0.15	6.08 ± 0.14	2.53 ± 0.06	2.40 ± 0.09	2.18 ± 0.10	0.27 ± 0.02
ADF22.A6	22:17:35.84	00:15:58.95	3.60 ± 0.12	3.20 ± 0.10	1.43 ± 0.04	1.63 ± 0.08	1.14 ± 0.07	0.14 ± 0.02
ADF22.A7	22:17:32.20	00:17:35.68	4.64 ± 0.12	4.17 ± 0.10	2.03 ± 0.04	1.78 ± 0.07	1.64 ± 0.07	0.22 ± 0.02
ADF22.A10	22:17:37.10	00:18:26.77	1.50 ± 0.09	1.68 ± 0.08	0.82 ± 0.05	0.46 ± 0.04	0.57 ± 0.05	0.11 ± 0.02
ADF22.A11	22:17:37.06	00:18:22.32	1.71 ± 0.11	1.67 ± 0.10	0.85 ± 0.03	0.60 ± 0.06	0.44 ± 0.05	0.09 ± 0.02
ADF22.A16	22:17:36.81	00:18:18.07	0.74 ± 0.10	0.46 ± 0.07	0.41 ± 0.06	0.06 ± 0.02	< 0.06	< 0.06

NOTE— Coordinates are measured with CASA/IMFIT using the $870\mu\text{m}$ maps at $0.5''$. Flux in the $1.1\mu\text{m}$ maps at $1.0''$ ($S_{1.1\text{mm},1.0''}$) are measured with CASA/IMFIT. For the remaining cases, fluxes enclosed with 2σ contours are measured. We also report the $1.1\mu\text{m}$ peak flux density at $0.05''$ ($S_{1.1\text{mm},0.05''}^{\text{peak}}$).

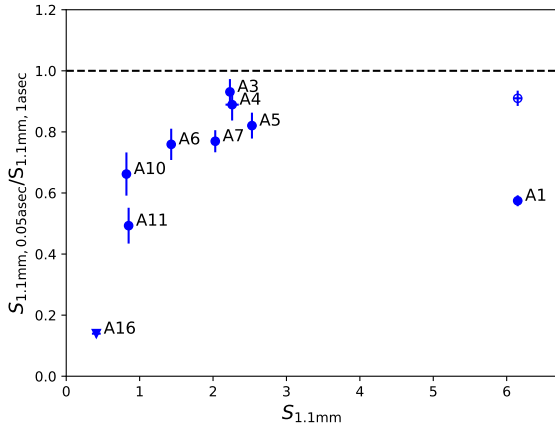


Figure 3. The 1.1 mm flux ratio between two angular resolutions ($S_{1.1\text{mm},0.05\text{asec}}/S_{1.1\text{mm},1\text{asec}}$) is shown as a function of the observed total 1.1 mm flux $S_{1.1\text{mm},1\text{asec}}$. The open circle represents the case of ADF22.A1 at $0.08''$. The fraction of recovered flux at $0.05''$ is broadly correlated with the total flux. This correlation may reflect differences in the intrinsic nature of dusty star-forming activity between bright and faint DSFGs, although we note several caveats.

ent as the resolution further increases and/or the total flux decreases.

Fig. 3 shows the 1.1 mm flux ratio between two angular resolutions ($S_{1.1\text{mm},0.05\text{asec}}/S_{1.1\text{mm},1\text{asec}}$), which represents the fraction of recovered flux at very high spatial resolution, as a function of the observed total 1.1 mm flux for each galaxy. Since the image at $1.0''$ has a slightly lower observed frequency (1.167 mm) compared to that of the high-resolution image (1.146 mm), we applied a correction factor (5%) to $S_{1.1\text{mm},1\text{asec}}$ in the calculation of the fraction, assuming modified blackbody radiation with $T_d = 30\text{ K}$ and $\beta = 2.0$.

One notable feature in the figure is the relatively low recovered fraction for ADF22.A1 compared to other bright DSFGs (ADF22.A3–ADF22.A7). This may be related to its exceptionally large size. As summarized in Table 3, the dust size of ADF22.A1 is $\gtrsim 2$ times larger than that of the other DSFGs. Assuming that both Band-6 and Band-7 data trace the same structure, its effective radius $R_e \approx 0.62''$ is comparable to the maximum recoverable scale of the C43-8 observation, suggesting extended flux is being resolved out.

On the other hand, there appears to be a correlation between the total flux and the recovered fraction for the remaining DSFGs. Fainter sources tend to show lower recovery rates. One possible explanation is a difference in the mechanisms powering the dust continuum emission: brighter SMGs may exhibit more compact emission structures, while fainter systems may be more

spatially extended. A caveat to this scenario is that fainter DSFGs inherently have lower signal-to-noise ratios, which could result in a lower fraction of significantly detected flux at a given threshold in the high-resolution image. Deeper imaging would help to better understand the underlying situation.

Overall, these results highlight the diverse spatial extents of dusty star-forming activity in galaxies, which are not solely concentrated into few dominant cores or clumps but are also distributed across extended disks. These trends are broadly consistent with previous works based on high-resolution dust continuum maps on sub-kpc scales (Iono et al. 2016; Hodge et al. 2016; 2019; Gullberg et al. 2018). It is reported that maps at $\gtrsim 0.15''$ tend to recover most of the flux (Hodge et al. 2016; Hodge et al. 2019), while maps at $\lesssim 0.05''$ often miss significant fractions of flux (Iono et al. 2016; Gullberg et al. 2018). We also note that there are some caveats in investigating flux recovery. The first caveat is that the recovery rate should highly depend on sensitivity. Another caveat is the use of the curve growth method. This method often results in “over-recovering” (e.g., Gullberg et al. 2018), possibly due to the contribution from the wing components of the synthesized beam and noise fluctuation, indicating that this effect may be prevalent (also for sources not showcasing over-recovering).

3.3. ALMA Profile Fit

The ALMA $870\ \mu\text{m}$ images taken at $0.15''$ have sufficient spatial resolution to identify internal structures on spatial scales comparable to those observed with JWST/NIRCam. They also preserve the sensitivity to detect relatively extended emission thanks to the inclusion of data from the compact array, as the flux recovery rate suggests. Hence we use these images to fit the surface brightness distribution of dust continuum emission in the DSFGs to quantitatively evaluate the profile of the dust continuum emission in these galaxies. We adopt a Sérsic profile (de Vaucouleurs 1948; Sérsic 1968), which is expressed as

$$I(r) = I_e \exp\left(-\kappa \left[\left(\frac{r}{r_e}\right)^{1/n} - 1\right]\right), \quad (1)$$

where $I(r)$ is the surface brightness at radius r , I_e is the surface brightness at the effective radius r_e , n is the Sérsic index that determines the concentration of the profile, and κ normalizes the profile such that the effective radius r_e corresponds to the half-light radius, enclosing half of the total flux of the source within r_e .

Table 3. ALMA 870 μm profile measurements

ID	Masked fits				Unmasked fits			
	n	Re [kpc]	b/a	P.A. [deg]	n	Re [kpc]	b/a	P.A. [deg]
ADF22.A1	0.94 ± 0.11	4.73 ± 0.53	0.42 ± 0.04	87.6 ± 8.8	3.78 ± 0.38	7.10 ± 1.07	0.33 ± 0.03	85.9 ± 8.6
ADF22.A3	1.0 ± 0.16	2.29 ± 0.23	0.36 ± 0.04	76.9 ± 7.8	0.67 ± 0.14	2.06 ± 0.23	0.16 ± 0.02	75.5 ± 7.6
ADF22.A4	1.27 ± 0.23	1.07 ± 0.15	1.0 ± 0.1	114.1 ± 100.5	2.04 ± 0.28	0.99 ± 0.15	0.86 ± 0.1	62.5 ± 12.6
ADF22.A5	0.71 ± 0.1	2.59 ± 0.31	0.36 ± 0.04	74.3 ± 7.5	1.43 ± 0.16	2.59 ± 0.31	0.2 ± 0.02	73.1 ± 7.3
ADF22.A6	0.73 ± 0.12	1.30 ± 0.15	0.72 ± 0.08	10.9 ± 4.0	1.42 ± 0.17	1.22 ± 0.15	0.63 ± 0.07	14.8 ± 4.3
ADF22.A7	1.01 ± 0.17	1.53 ± 0.15	0.58 ± 0.06	17.4 ± 2.5	1.7 ± 0.22	1.45 ± 0.15	0.4 ± 0.04	18.4 ± 2.4

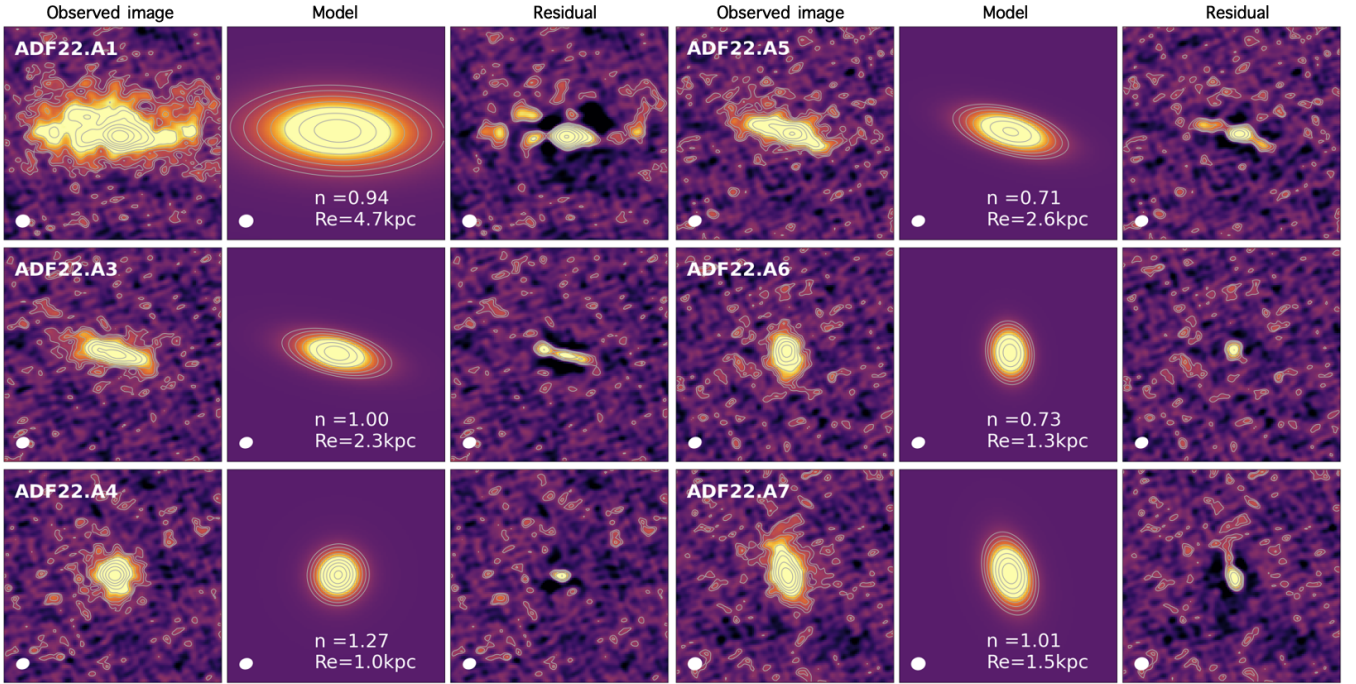


Figure 4. Results of the profile fit with ALMA 870 μm imaging on the six brightest DSFGs in ADF22 (0.15'' resolution). From left to right, each panel shows the observed images, the best-fit Sérsic profile, and the residual maps. Each panel is $2.4'' \times 2.4''$ ($18.3 \times 18.3 \text{ kpc}^2$) in size. Contours are $\sigma \times 1.5^n$, with $n = 1$ to $n = 10$. We obtained the best-fit models (and residuals), masking residual pixels $> 5\sigma$ iteratively as described in §3.3. Central cores and other substructures, suggestive of bars and clumps, are unveiled, together with the existence of disk profiles on a galaxy scale.

First we fit a two-dimensional Sérsic surface brightness profile, allowing the effective radius r_e , source position, axial ratio, position angle, and Sérsic index n to vary. To account for the beam convolution effect, the model is convolved with the synthesized beam, characterized by its semimajor axis, semiminor axis, and position angle as provided by the beam parameters of each map. Following the recipe presented by Hodge et al. (2019), we performed the fit by iteratively masking residual pixels above 5σ until the masks converged. This step is suitable to appropriately characterize disk components in the presence of clumpy structures. This technique also

ensures that any real positive structure in the disks does not artificially boost the fits of the underlying smooth profiles, which could otherwise perturb the results causing large negative troughs in the residual images (Hodge et al. 2019). We also measured these parameters without masks to parameterize the whole profile including a concentrated core.

The best-fit models and residual maps for the six brightest DSFGs in ADF22 are shown in Fig. 4. The derived parameters are summarized in Table 3, while the representative values of Sérsic index and effective radius are also noted in the panels in Fig. 4. The derived Sérsic

index for the six bright DSFGs is $\langle n \rangle = 0.86 \pm 0.05$ when we applied the bright emission masks. This suggests that an exponential disk profile is a common feature of the DSFGs. Hodge et al. (2016) reported similar values for DSFGs in a general field of similar redshifts using comparable resolution images ($\langle n \rangle = 0.9 \pm 0.2$), which indicates that such disk profiles of dust continuum emission are common characteristics among DSFGs in various environments. The Sérsic index increases when bright emission masks are not used ($\langle n \rangle = 1.37 \pm 0.08$). This suggests that the DSFGs have an extra component concentrated into a core, which is also recognizable in the residual maps and detections in the 1.1 mm maps with higher angular resolutions. An exception is ADF22.A3, which shows $n = 0.67 \pm 0.14$ without masks (while it has $n = 1.00 \pm 0.16$ with masks). One possible explanation is that a bar, which tends to have a flatter profile, dominates the bright part.

The effective radius for the six DSFGs ranges from $0.14''$ to $0.62''$ (1.06 to 4.73 kpc), showcasing a variety of the disk sizes as reported by previous works for general field DSFGs (e.g., Gullberg et al. 2019). There is also an exception. ADF22.A1 has a remarkably large dust disk ($r = 0.62''$, 4.73 kpc) also associated with large gas and stellar disks (Umehata et al. 2024), which is larger than any of previously known samples observed at a comparable resolution (Gullberg et al. 2019). The special environment, associated with gas filaments in the proto-cluster core, can account for such a huge disk (Umehata et al. 2024). A remarkable finding is the prevalence of substructures in the bright DSFGs. This could reflect bulges, bars, and clumps in spiral arms, as also reported by Hodge et al. (2019) for DSFGs in general fields. We will discuss the origin more in §5.1 together with NIRCam data and ALMA Band-6 images at $0.05''$ – $0.08''$.

As a test, we refit the sample with a fixed n ($n = 1$) without masking. The results are shown in Fig. A1. For the six bright DSFGs, this fit broadly yielded similar parameters compared with the fit with bright emission masks. This may be reasonable since the derived Sérsic index with masks are close to $n = 1$. In the following, we take the fits with masks as our primary estimates. For two faint sources detected near the primary targets, ADF22.10 and ADF22.11, fit with a Sérsic index of $n = 1.0$ work well (see Appendix), while this assumption is necessary due to the low significance of the detected emission. The final source ADF22.A16 was excluded from all fits since it is too faint at this resolution (Fig. 2).

We note that high fidelity data is required for high resolution profile fits which also need to capture extended emission from disks. This is showcased in our data

set. The ALMA Band-6 data is sensitive to compact emission but does not have sufficient sensitivity for disk profile characterizations. In these data one-component fits without masks sometimes resulted in high n values ($n \gtrsim 5$). This does not mean that the galaxy does not have dust continuum emission from a disk (this is caused by the lacking of the sensitivity for extended components), as also suggested by stacking analysis by Gullberg et al. (2019). However, such high-resolution images offer a finer views of the galactic structures, which is useful to resolve small scale structures.

4. STELLAR MORPHOLOGIES AND COMPARISON WITH DUST CONTINUUM

4.1. Stellar and dust emission in DSFGs

The JWST/NIRCam images provide the opportunity to resolve the internal structures of DSFGs and associate them with dust continuum emission. Fig. 5 shows the images in the individual NIRCam filters. A notable trend is that a significant fraction of DSFGs are heavily obscured, rendering most regions invisible in the bluer bands even in the K_s -band (F200W). This trend highlights that a wavelength of approximately 5000 \AA in the rest frame is too short to effectively trace stellar emission even from massive galaxies in such a dusty population at $z \sim$. While this wavelength is often considered suitable for deriving stellar mass distributions due to its inclusion in the rest-frame optical regime, its limitations in dusty systems must be acknowledged.

In Fig. 6, we presents a side-by-side comparison of NIRCam color images, which combine data from the F200W, F356W, and F444W filters, and $870 \mu\text{m}$ maps for proto-cluster DSFGs. This reveals a striking diversity in the size, color, inclination, and structure of the DSFGs. In most cases (eight out of nine DSFGs), the peaks of $870 \mu\text{m}$ emission broadly coincide with those of the rest-frame $\sim 1.1 \mu\text{m}$ emission in the F444W images at the $\sim 0.15''$ resolution. This indicates that we are beginning to directly capture stellar mass assembly in the central regions of galaxies, where dust extinction is most severe (Gillman et al. 2024; Hodge et al. 2025). The exception is ADF22.A7, which shows an offset between the peaks of $870 \mu\text{m}$ and F444W emissions. This offset is intrinsic and not due to astrometric uncertainties (both A1 and A7 are in the same single FoV of ALMA Band7/Band6 observations, and astrometry is calibrated across the ADF22 field). We will discuss the nature of this DSFG in §5.3.

The bluer band images (F115W and F200W, $\sim 2800 \text{ \AA}$ and $\sim 4900 \text{ \AA}$ in the restframe) also provide several new insights. Some DSFGs, such as ADF22.A1 and ADF22.A10, exhibit blue arms in their outskirts,

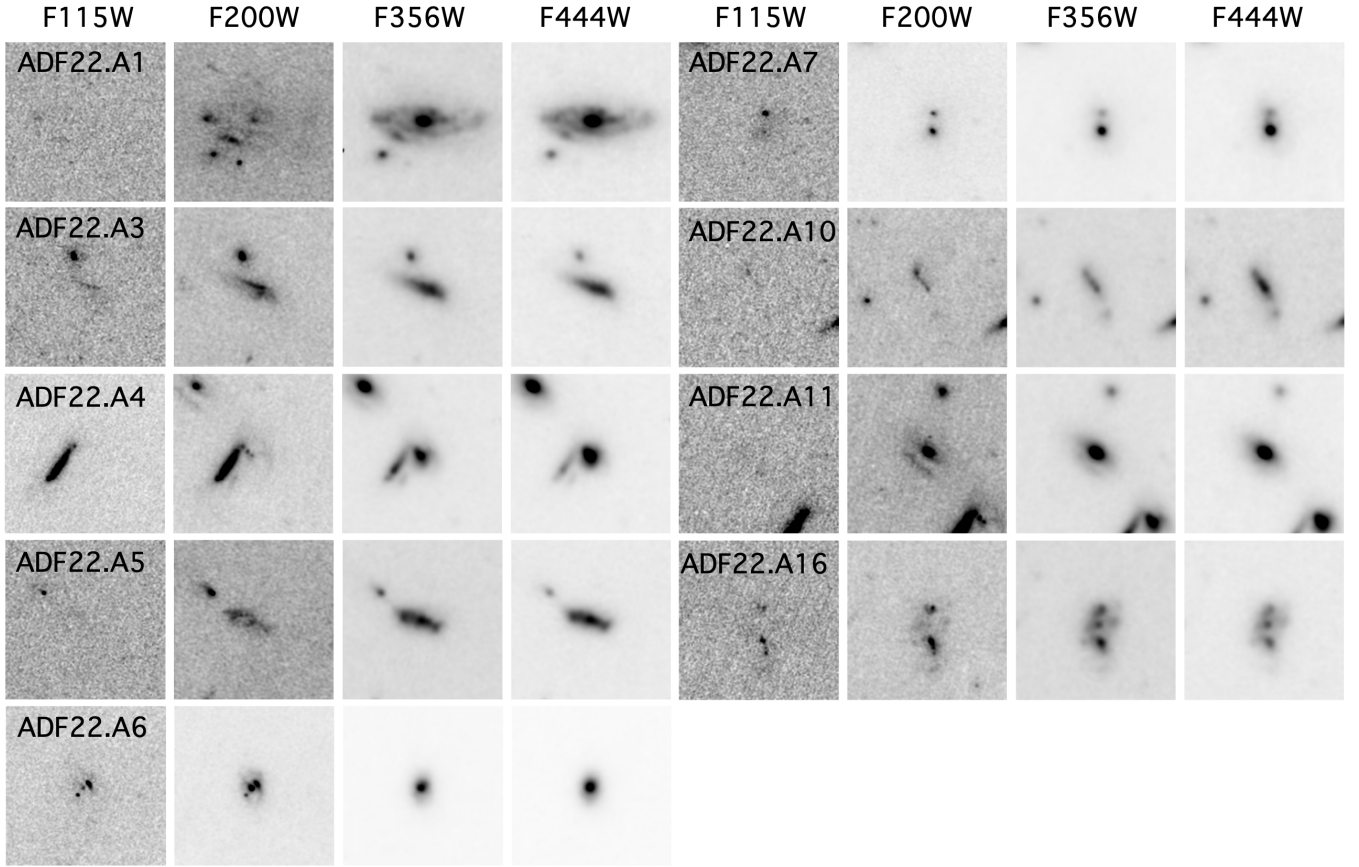


Figure 5. Postage stamps of the NIRCcam images as marked. Each panel is $3.8'' \times 3.8''$ ($29 \times 29 \text{ kpc}^2$ at $z = 3.09$) in size. Dust extinction is severe in bluer bands (F115W and F200W).

suggesting the presence of less dusty regions within these DSFGs as well as inhomogeneous dust obscuration across their disks. Several clumps are visible in the shorter wavelength images, as exemplified by ADF22.A4 and ADF22.A6 (Fig. 5, see also Fig. B1 in Appendix). These features are not detectable in the F356W/F444W maps, likely due to their intrinsically blue (and lower masses) nature and/or the lower resolution of the longer wavelength images. The blue clumps that spatially overlap with the $870 \mu\text{m}$ (and F444W) emission possibly reflect nuclear activity, including nuclear starbursts and AGNs (both DSFGs host X-ray-detected AGNs, while their SEDs are dominated by galaxies (Monson et al. (2023))). The remaining clumps may represent young star clusters, similar to the UV clumps observed by HST in $z = 1 - 2$ galaxies (e.g., Conselice et al. 2004; Elmegreen & Elmegreen 2005; Elmegreen et al. 2007; 2009; Bournaud et al. 2008; Genzel et al. 2008; 2011).

4.2. NIRCcam Profile Fit

The NIRCcam F444W images were utilized to characterize morphologies in stellar emission since they provide the longest wavelength coverage among the NIRCcam data. The rest-frame wavelength at $z = 3.09$ is approximately $1.1 \mu\text{m}$, corresponding to the rest-frame near-infrared. Thus, the F444W image is optimal for tracing stellar structures among the available images, while we note that the rest-frame wavelength may still be affected by dust extinction (e.g., Hodge et al. 2025; Umehata et al. 2024).

We fit a Sérsic profile to the F444W surface brightness of individual DSFGs using GALFIT (Peng et al. 2002, 2010). The input files for the GALFIT analysis include a science image, a PSF map, a sigma map, and a mask map. For the F444W image, we use the original pixel scale ($0.063'' \text{ pixel}^{-1}$) without applying drizzling, and we create $150 \text{ pixel} \times 150 \text{ pixel}$ thumbnails centered on each DSFG. We obtain the most realistic PSFs following previous studies (Chen et al. 2022; Hodge et al. 2025). Using WebbPSF (Perrin et al. 2014), we generated a PSF matched to in-flight JWST data. We use the PSF simulated for our instrument setup and date

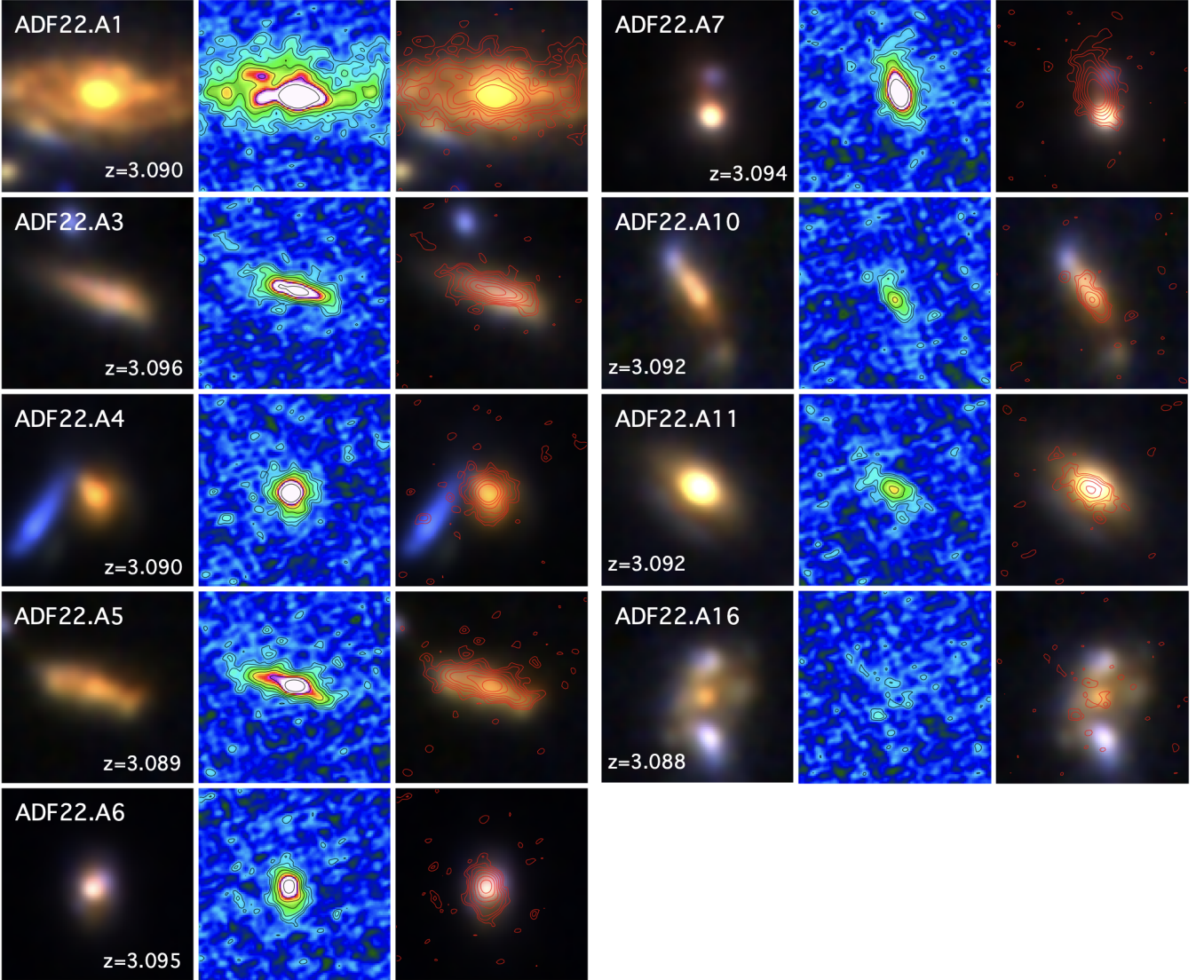


Figure 6. A combined ALMA and JWST views of nine DSFGs. (left) NIRCcam pseudo-color images (blue: F200W, green: F356W, red: F444W) for the nine proto-cluster DSFGs in ADF22, in which PSF sizes are matched to that of F444W. Each panel is $2'' \times 2''$ in size. (middle) ALMA $870\mu\text{m}$ images. Contours represent $\sigma \times 1.5^n$ ($n=2$ to 11) of the $870\mu\text{m}$ emission. (right) NIRCcam images with the ALMA contours. JWST/NIRCcam reveals diverse stellar colors and morphologies among the DSFGs. The dust continuum emission observed with ALMA is broadly coincident with the stellar light.

of observation. The charge diffusion sigma option of the WebbPSF is adjusted to fit the PSF to nearby unsaturated stars. The input image values are converted to have units of count rate and the sigma image is generated internally by GALFIT. The mask image is generated using SEXTRACTOR (Bertin & Arnouts 1996). Sources detected with > 1.5 sigma for > 12 adjacent pixels are extracted and masked. Measurements are iterated 1000 times with a range of initial values, which finally provides the representative values and errors as median and standard deviation. We estimate the errors for each output parameter by adding a 10% fractional uncertainty in quadrature to all parameters, following the approach

of Hodge et al. (2025). Fig. 7 shows the best-fit model and residual images, together with the observed F444W images, for the six bright ADF22 DSFGs. Similar to $870\mu\text{m}$ image, fits with GALFIT are also performed with a fixed $n = 1$. The derived parameters are summarized in Table 4.

4.3. Comparison between ALMA and JWST profiles

The derived parameters characterizing the dust and stellar emission profiles are compared in Fig. 8. For reference, we also include measurements from $z \sim 3$ DSFGs originally identified in the general field from Hodge et al. (2025). The Sérsic index, n , show moderate correlation within the range of $n \sim 1 - 2$ in most cases. The galax-

Table 4. NIRCcam F444W profile measurements

ID	Free n fits				Fixed $n = 1$ fits			
	n	Re [kpc]	b/a	P.A. [deg]	n	Re [kpc]	b/a	P.A. [deg]
ADF22.A1	1.61 ± 0.17	6.68 ± 0.69	0.39 ± 0.04	89.8 ± 8.9	1.00	5.86 ± 0.60	0.39 ± 0.04	89.8 ± 8.9
ADF22.A3	0.71 ± 0.09	3.49 ± 0.37	0.31 ± 0.03	68.9 ± 6.9	1.00	3.77 ± 0.39	0.30 ± 0.03	68.7 ± 6.9
ADF22.A4	1.59 ± 0.29	1.81 ± 0.19	0.86 ± 0.11	48.2 ± 9.2	1.00	1.60 ± 0.16	0.86 ± 0.09	46.7 ± 5.2
ADF22.A5	0.36 ± 0.04	3.28 ± 0.34	0.31 ± 0.04	73.5 ± 7.3	1.00	3.76 ± 0.39	0.30 ± 0.03	73.4 ± 7.3
ADF22.A6	1.43 ± 0.38	1.50 ± 0.15	0.69 ± 0.13	-4.9 ± 17.5	1.00	1.41 ± 0.14	0.70 ± 0.11	-5.2 ± 11.2
ADF22.A7	3.21 ± 0.37	2.24 ± 0.25	0.54 ± 0.06	10.6 ± 1.2	1.00	1.55 ± 0.17	0.57 ± 0.07	10.5 ± 1.2
ADF22.A10	1.14 ± 0.14	3.33 ± 0.38	0.28 ± 0.06	27.8 ± 4.9	1.00	3.22 ± 0.37	0.28 ± 0.05	27.9 ± 3.7
ADF22.A11	3.51 ± 0.46	2.83 ± 0.30	0.54 ± 0.08	54.1 ± 12.1	1.00	1.62 ± 0.17	0.57 ± 0.07	55.0 ± 5.9
ADF22.A16	0.42 ± 0.11	3.80 ± 0.50	0.44 ± 0.07	-3.3 ± 5.8	1.00	4.17 ± 0.60	0.41 ± 0.05	-3.4 ± 6.6

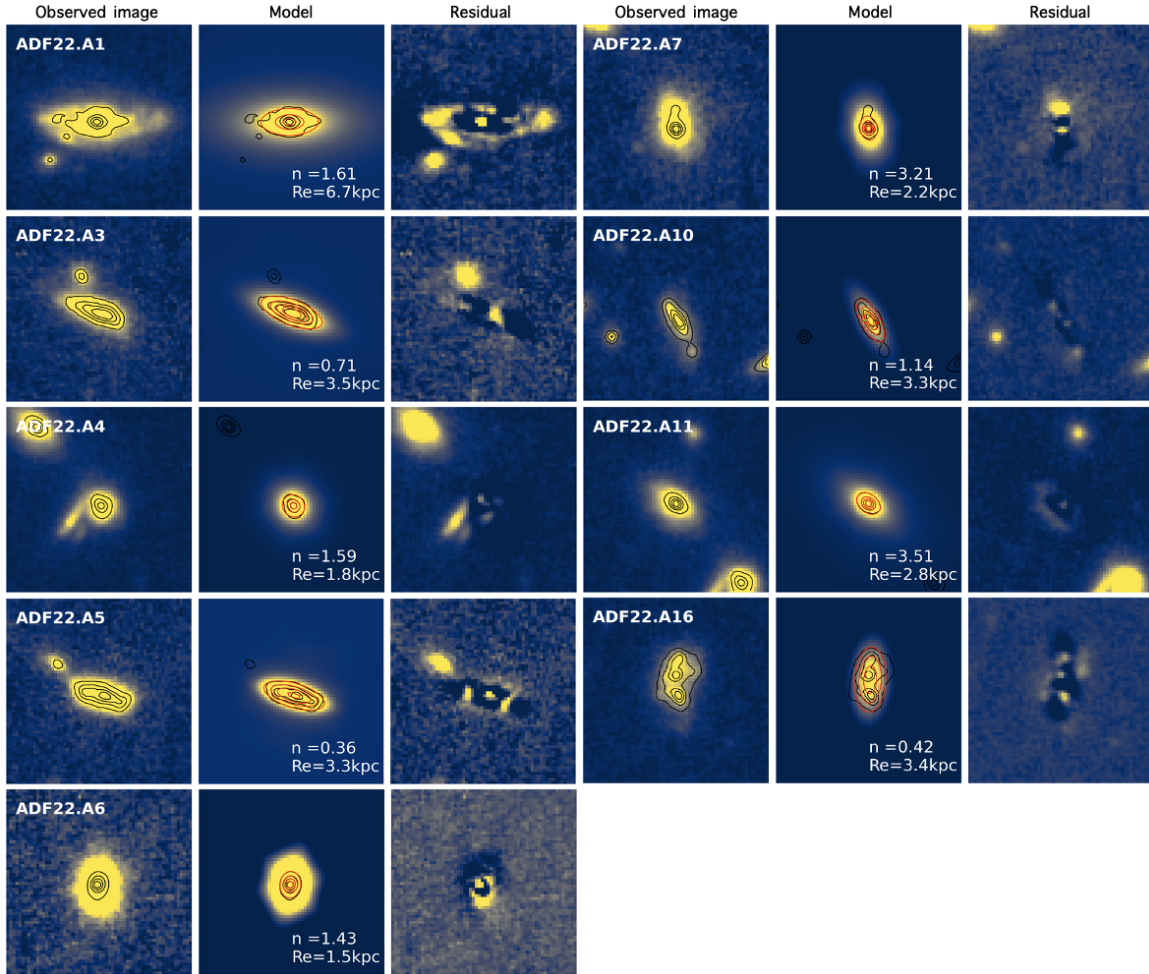


Figure 7. Postage stamps of JWST NIRCcam F444W images for the nine DSFGs in ADF22 ($30 \times 30 \text{ kpc}^2$ in size). As in Fig. 4, each panel from left to right displays the observed image, the best-fit Sérsic profile, and the residual map. Black (red) contours represent 20%, 40%, 60%, and 80% of the peak flux of the observed (modeled) images. The majority of the profiles tend to show $n > 1$, suggesting the presence of a forming bulge.

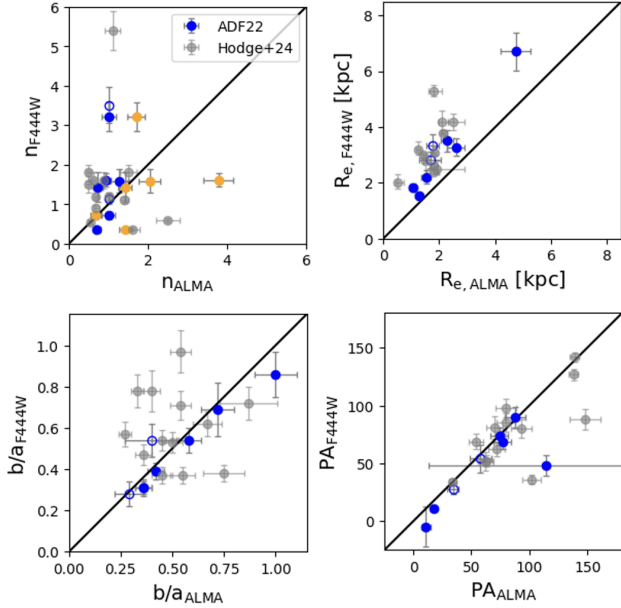


Figure 8. Comparison of parameters derived by profile fit on ALMA $870\ \mu\text{m}$ and JWST NIRCcam F444W images. Blue filled circles show the results from ALMA profile fit with the bright source masks, while yellow circles show the results without the masks (only in the top right panel). Open blue circles shows ADF22.A10 and A11, whose measurements were obtained with $n = 1$ and adopting no masks. For comparison, measurements from previous works (Hodge et al. 2025) also plotted. The axis ratios and position angles measured by the two ways show good consistency, supporting the scenario that dust emission comes from across disks.

ies with $n_{\text{F444W}} > 1$ can be interpreted as a mixture of disks and central spheroidal components. There are two sources with $n_{\text{F444W}} < 1$ (ADF22.A3 and ADF22.A5), which may be attributed by flattened profile due to significant dust extinction and/or possibly bars. If bright emission masks were not applied, n_{ALMA} would exhibit larger values, reflecting the influence of bright and relatively compact cores in dust emission of some sources. A similar situation likely applies to F444W, where we conservatively adopted a single-component fit due to the limited sensitivity. There is an exception, ADF22.A7, which shows a remarkable discrepancy between the two types of measurements. We discuss this source more in §5.3.

For the effective radius, R_e , the F444W measurements tend to be larger than those of dust, although a positive correlation exists between the two. This trend is broadly consistent with previous studies (e.g., Chen et al. 2022; Hodge et al. 2025; Gillman et al. 2024). Notably, the trend remains unchanged when adopting the effective radius measured with a fixed Sérsic index ($n = 1$). From the perspective of hydrodynamical simulations, Popping

et al. (2022) predicted smaller stellar mass sizes compared to $850\ \mu\text{m}$ sizes in massive star-forming galaxies at $z = 1-5$. On the other hand, observational studies have reported the opposite behavior in observed sizes measured at submillimeter wavelengths and F444W (e.g., Chen et al. 2022; Gillman et al. 2024). Several factors could contribute to this apparent contradiction. For instance, simulations may require improvements in accounting for details of central mass growth and obscuration associated with bulge formation. It should be also noted that F444W measurements can still be affected by dust extinction, which may flatten the observed profiles (decreasing the measured n). As a result, the intrinsic stellar mass profile could be more compact than it appears in F444W images.

We can see good consistency between the ALMA and F444W measurements on the b/a ratio and position angle (PA). This result is inline with the idea that dust emission generally originates from across disks. To evaluate the relationship between the parameters derived from the F444W and $870\ \mu\text{m}$ data, we compute the Pearson correlation coefficient (ρ) following Hodge et al. (2025), which quantifies the strength of a linear monotonic association between two datasets, for the six brightest DSFGs. The resulting values of ρ (along with their corresponding probabilities) are 0.37 (0.47) for n , 0.99 (0.00) for R_e , 0.99 (0.00) for b/a , and +0.79 (0.06) for PA. The results again indicate the significant correlation except for the Sérsic index.

The results and trends shown in Fig. 8 are broadly consistent with those for DSFGs in general fields reported by Hodge et al. (2025) (see also Gillman et al. 2024). However, a notable exception arises in the case of the axis ratio. While they found no correlation between the ALMA and F444W measurements for the axis ratio, the ADF22 DSFGs exhibit a clear correlation. Since all of the DSFGs presented in this paper are located in the proto-cluster core, this might be linked to the formation process preferentially occurred in the biased environment (we will revisit this point in the next section). Furthermore, the comparison between the two studies highlights the unique large stellar and dust sizes of ADF22.A1 in the proto-cluster core (Umehata et al. 2024).

5. DISCUSSION

5.1. The origins of dust continuum emission

Multi-scale ALMA submm images, combined with rest-frame optical to near-infrared NIRCcam images, provide critical insights into identifying the structures responsible for dust emission in galaxies on a resolved scale. The emission, after masking the bright regions,

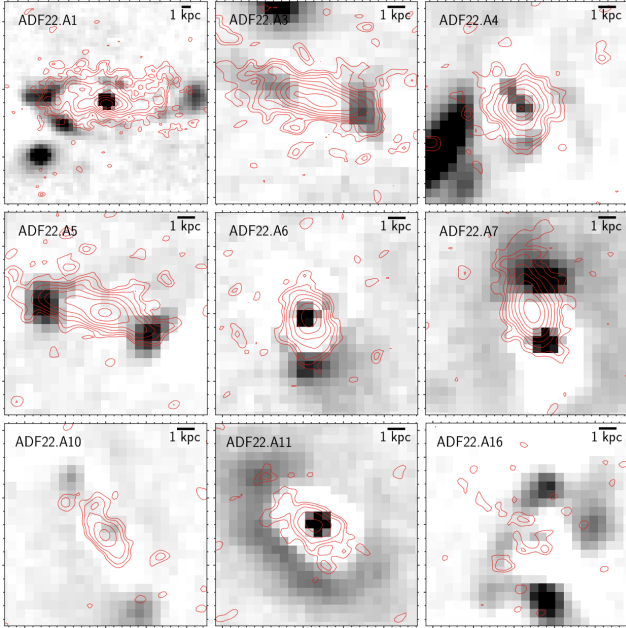


Figure 9. The F444W residual images after subtracting the best-fit Sérsic model with a fixed Sérsic index ($n = 1$). The contours represent the $870\ \mu\text{m}$ emission at $0.15''$, as shown in Fig. 1. The peaks of the dust continuum often coincide with the central residuals of the F444W emission, suggesting the co-existence of stellar spheroids and central starbursts in the DSFGs.

is well characterized by a disk-like profile, with the axis ratios and position angles showing good consistency, as described above. These observational clues suggest that the dust continuum originates predominantly across disks in DSFGs. This interpretation is supported by the stacked detection of faint and extended components reported by Gullberg et al. (2019). The dust emission is also characterized by dominant bright cores, a feature reported in numerous previous studies (e.g., Simpson et al. 2015; Ikarashi et al. 2015; Hodge et al. 2016; Gullberg et al. 2019; Tan et al. 2024). The NIRC*am* images now reveal that these cores are situated at the centers of disk-like galaxies. Fig. 9 compares the the F444W residual images, which is obtained subtracting a $n = 1$ best-fit model, with the $870\ \mu\text{m}$ emission at $0.15''$ for the nine ADF22 DSFGs at $z \approx 3.09$. A notable feature is that about a half of the F444W residual image have residuals at the center, which corresponds the peak of the dust continuum emission (ADF22.A1, A4, A6, A11). This result suggests concurrent starburst activity and, to a certain extent, the presence of mature stellar bulges. Similar situation can be found in other DSFGs in a general field, such as ALESS3.1 at $z = 3.375$ (Hodge et al. 2025), and hence can be a general nature of DSFGs. This point will be explored further below.

Another notable feature is that the combination of disks and cores alone is insufficient to fully characterize the observed profiles. One key characteristic is the presence of dusty bars (Hodge et al. 2019; Tsukui et al. 2024), most prominently seen in ADF22.A1 (Umehata et al. 2024). ADF22.A3 and ADF22.A5 also exhibit similar elongated structures in the high-resolution dust emission images at $0.08''$ (Fig. 1) and residual images (Fig. 4), which reveal structures resembling the offset ridges in local barred galaxies. These may reflect the prevalence of bars in DSFGs (e.g., Smail et al. 2023; Amvrosiadis et al. 2024), though kinematic data may be required to confirm this scenario, as demonstrated for ADF22.A1 (Umehata et al. 2024), and it is also required to expand the sample size. There are no clear counterparts for these bars (or bar-like features) in the NIRC*am* images (e.g., Fig. 9). The most significant cause would be dust obscuration, could easily obscure bar structures in DSFGs (Simpson et al. 2017; Hodge et al. 2025; Umehata et al. 2024). An intriguing feature is the Sérsic indices of the two DSFGs, ADF22.A3 and ADF22.A5. These exhibit $n < 1$ in the F444W profile fit. The flattened emission profiles may result from significant dust extinction, as discussed above, but could also be caused by the presence of bars. Bars can exhibit have lower Sérsic indices in local galaxies (e.g., Kruk et al. 2018). Both DSFGs exhibit an edge-on-like geometry, and if bars dominate the stellar emission, the measured Sérsic indices could fall below unity. It is prevalent for inclined disk galaxies to exhibit pairs of F444W residuals near the edge of the $870\ \mu\text{m}$ emission (e.g., ADF22.A1, A3, A5, A10; see Fig. 9). As demonstrated in the case of ADF22.A1, this can be associated with stellar spiral arms.

Additional dusty clumps (not in the core) are observed in ADF22.A1 (Fig. 1, Fig. 4), suggesting that such clumps, alongside cores and bulges, exist in at least some DSFGs (Iono et al. 2016; Tadaki et al. 2018; Hodge et al. 2019), while we need more data to derive their prevalence and nature. In summary, the dust continuum emission observed in DSFGs cannot be described by simple structures, such as a single compact bright component, but is instead attributed to multiple substructures, including disks, cores, bars, and clumps.

5.2. Bulge formation and morphological transformation in DSFGs

Leveraging the unique advantage of our observations that the DSFGs are well-resolved in both stellar and dust continuum emission, we aim to bridge these two perspectives to shed light on the process of bulge formation. One particularly exciting discovery is the presence

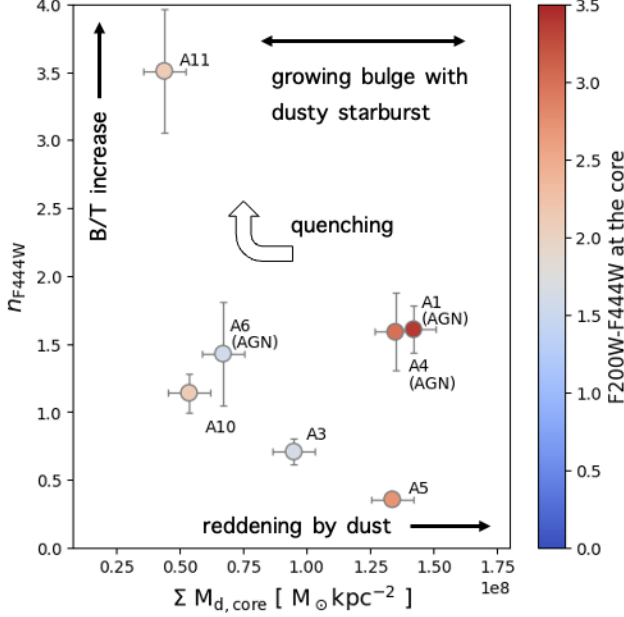


Figure 10. The relation among dust mass surface density at the core ($\Sigma M_{d,\text{core}}$), Sérsic index measured for the F444W image (n_{F444W}), and F200W-F444W color at the core. Dusty starburst at the core, which causes severe dust reddening, would correspond to the rapid growth phase of bulges.

of compact dusty cores in the bright DSFGs, which are strikingly prominent at a resolution of 350 pc (Fig. 1). To quantify this, we estimated the dust mass surface density at the core using the $0.05''$ resolution 1.1 mm images, as described below:

$$\Sigma M_{d,\text{core}} = \frac{S_{\nu_{\text{obs},0.05''}} D_L^2 (1+z)^{-(3+\beta)}}{\kappa(\nu_{\text{ref}}) B_\nu(\nu_{\text{ref}}, T_d) A_{\text{beam}}} \left(\frac{\nu_{\text{ref}}}{\nu_{\text{obs}}} \right)^{2+\beta} \quad (2)$$

Here, $S_{\nu_{\text{obs},0.05''}}$ is the peak flux density measured at $0.05''$ resolution, and D_L is the luminosity distance. The terms ν_{ref} and ν_{obs} represent the reference frequency and observed frequency, respectively. We adopt a spectral emissivity index of $\beta = 1.8$, a dust mass absorption coefficient at $850 \mu\text{m}$ of $\kappa(\nu_{850}) = 0.04 \text{ m}^2 \text{ kg}^{-1}$ (Li & Draine 2001), and a mass-weighted dust temperature of $T_d = 25 \text{ K}$ (Scoville et al. 2016). The term $B_\nu(\nu_{\text{ref}}, T_{\text{dust}})$ denotes the Planck function, and A_{beam} is the beam solid angle. The effect of the cosmic microwave background (CMB) is not corrected for, as it is not dominant at the studied redshift (da Cunha et al. 2013).

To evaluate the reddening effect, we also performed photometry at the core using an aperture centered on the dusty core with $d = 0.15''$ and measured the color F200W-F444W in AB magnitude. Together with the Sérsic index measured for the F444W image (n_{F444W}),

we plot the relation among the three parameters: dust mass, stellar morphology, and reddening in rest-frame optical-to-near-infrared color, in Fig. 10. ADF22.A7 is excluded since the configuration of dust and stellar emission is complicated in this DSFG.

One trend we can see in the diagram is the correlation between dust mass surface density and color. The three DSFGs, ADF22.A1, A4, and A5, hosting the brightest dusty cores, show the reddest color, highlighting that dust obscuration is a primary cause of the reddening of the SED in this wavelength range (Gillman et al. 2024; Hodge et al. 2025). Two of them (ADF22.A1 and A4) also show relatively high Sérsic indices, $n_{F444W} \approx 1.5-2$. Together with the spatial overlap of core emissions between the dust and stellar components (Fig. 6), this indicates that the DSFGs may have already assembled significant stellar mass in the proto-bulge, while the phase of bursting growth is still ongoing. The low index, $n_{F444W} \lesssim 0.5$, observed in ADF22.A5 can be attributed to a combination of (i) severe dust extinction, (ii) relatively immature stellar mass in the proto-bulge, and (iii) a possible bar structure. Although it is challenging to distinguish these scenarios at the moment, the growth of proto-bulges may increase n values during the DSFG phase. The result also suggests that the near-infrared-dark nature observed in some DSFGs (e.g., Simpson et al. 2014; Umehata et al. 2020; Ikarashi et al. 2022) is associated with the rapid growth phase of bulges (Smail et al. 2021).

Interestingly, ADF22.A1 exhibits a bar structure identified in both dust and [C II] emission (Umehata et al. 2024), and ADF22.A5 also shows signatures of offset ridges in the dust continuum (Fig. 1). These clues suggest that bars play a key role in driving gas to the central regions, fueling mass growth in the core and triggering dusty starburst activity. It is also found that the brightest, compact dusty cores are not ubiquitous among DSFGs. In the ADF22 sample, ADF22.A3 and A6 exhibit lower dust mass surface densities and consequently show slightly more moderate reddening in their colors. This diversity might reflect different stages along a similar evolutionary path (i.e., they are relatively immature and will develop bursty cores in the future, or they previously hosted the brightest cores but have now transitioned out of the rapid growth phase), or it could indicate multiple channels for DSFG formation (e.g., bypassing the bursty phase entirely). Statistical samples and detailed analyses of SEDs will help clarify these scenarios.

There are three DSFGs hosting a X-ray AGN (ADF22.A1, A4, A6) in Fig. 10 (note that we excluded ADF22.A7, another AGN-host DSFG, in the analysis).

The fact that both of ADF22.A1 and A4 host (heavily obscured) X-ray AGNs support the idea that growth of bulges and SMBHs are simultaneously accelerated in the most intense phase. With the limited samples in our hand, it is not straightforward to discuss the role of AGNs in quenching.

In Fig. 10, ADF22.A11 occupies a unique parameter space. Its F444W Sérsic index is close to the de Vaucouleurs profile, characteristic of local elliptical galaxies (de Vaucouleurs 1948). ADF22.A11 could be in a transitional stage from DSFGs to quiescent galaxies (QGs), as also suggested by its position in the transitional rest-frame UVJ diagram (Kubo et al. 2016; Kubo et al. in preparation). On the other hand, significant dust emission is still detected. The dust emission profile is well described by an $n \simeq 1$ model (Fig. A1) with no signature of a dense dusty core. An explanation consistent with these observational clues is that inside-out quenching is occurring, where star formation activity has ceased in the innermost regions (resulting in the $n \sim 4$ feature being visible only in the F444W profile, while the dust emission at very high resolution becomes faint), while star formation in the disk has not yet fully quenched. Such a transitional phase may have a short duration, with DSFGs generally following the evolutionary track suggested in Fig. 10, which could explain why only ADF22.A11 is identified in the ADF22 sample.

5.3. Environment and evolution

The ADF22 field is situated in the heart of the SSA22 proto-cluster (Umehata et al. 2015), with the DSFGs ubiquitously embedded within the cosmic web filaments traced by Ly α emission (Umehata et al. 2019). In this section, we aim to connect the derived properties discussed above with this specific environment.

The NIRCcam images, including F444W, reveal that the stellar mass distributions of DSFGs are generally characterized by a disk-like profile, similar to local late-type galaxies. The spatial locations of dust emission broadly align with those of the stellar components. These results indicate that DSFGs in the proto-cluster core are predominantly disk galaxies (Umehata et al. 2024). This finding contrasts sharply with the well-established local morphology-density relation, where spheroidal galaxies dominate cluster centers while late-type disk galaxies are preferentially distributed in the surrounding, less dense environments (Dressler 1980). Theoretical models suggest that phase space is conserved during the hierarchical collapse of structures, implying that the densest regions at high redshift will correspond to the densest regions in their descendants in the local universe. Hence, we are witnessing the origin

of the morphology-density relation in the early universe, where the ancestors of local massive elliptical galaxies are undergoing a growth phase, rapidly assembling their mass as disk galaxies in proto-clusters. While this work sheds light on the situation for massive galaxies in the core of the proto-cluster, it presents an intriguing opportunity to further explore the outskirts of $z \sim 3$ proto-clusters and/or less massive systems. Characterizing these regimes and redshift evolution will provide a more comprehensive understanding of galaxy evolution in proto-cluster environments.

To explain the high levels of star-formation activity observed in DSFGs, several scenarios have been proposed to effectively supply and consume gas fuel for this population, including cold gas accretion from the cosmic web (Dekel & Birnboim 2006; Dekel et al. 2009) and major/minor mergers (e.g., Hopkins et al. 2006). The morphologies revealed by NIRCcam and ALMA images may support the scenario that the starbursts in the proto-cluster DSFGs are predominantly driven by minor perturbations or in-situ processes, such as disk instabilities (e.g., Tadaki et al. 2018), possibly fueled by the abundant gas supply from the cosmic web (Umehata et al. 2019). For example, ADF22.A1 has a Toomre- Q value below unity and exhibits a highly spun-up disk, consistent with an in-situ channel (Umehata et al. 2024). While the high density of DSFGs and neighboring galaxies suggests elevated rates of major and minor mergers, which likely play significant roles in their mass assembly, individual DSFGs in the starburst phase display morphologies reminiscent of late-type galaxies albeit disordered examples. This indicates that major mergers may not necessarily be the primary driver of starburst activity in these systems.

The configuration of ADF22.A7 is not straightforward to interpret. Photometric redshifts derived from non-resolved photometry support the idea that the system as a whole is at $z \sim 3.09$ (Umehata et al. 2014; Umehata et al. 2015), which is also consistent with the CO detections (Umehata et al. 2019; Rizzo et al. 2023; H. Umehata et al., in preparation). Meanwhile, the NIRCcam images reveal two peaks, neither of which aligns with the dust peak. The NIRCcam color image presents an extra red component at the dust position, though (Fig. 6). This suggests the possibility of a superposition of proto-cluster galaxies along the line of sight. Follow-up observations, such as those with JWST/NIRSpec-IFU, will help clarify the nature of this system.

6. CONCLUSIONS

We have presented high-resolution imaging of nine dusty star-forming galaxies (DSFGs) in the $z = 3.1$

SSA22 proto-cluster, observed with both ALMA and JWST. These observations, reaching angular resolutions as fine as $0.05''$ at 1.1 mm, unveil the internal structures of DSFGs down to sub-kpc scales. The ALMA images reveal intricate spatial distributions of dust continuum emission, including compact dusty cores, elongated features suggestive of bars, and clumpy structures on scales down to ~ 350 pc. Meanwhile, JWST/NIRCam observations provide unprecedented views of the stellar structures in these galaxies, also including three faint DSFGs in the vicinity of the bright ADF22.A4. For the first time, these observations reveal the internal stellar morphology and rest-frame optical-to-near-infrared colors of DSFGs in proto-clusters in detail.

The surface brightness distributions of six bright DSFGs were fit with Sérsic profiles, utilizing ALMA $870 \mu\text{m}$ and JWST F444W images. Both datasets suggest the existence of disk-like profiles in general, with Sérsic indices ranging from $n \sim 1$ to $n \sim 2$ broadly. This range is consistent with a mixture of extended disks and central spheroidal components. The axis ratios, and position angles derived from the ALMA and JWST F444W data show good agreement, supporting the idea that dust continuum emission originates across the disk. The effective radii at $870 \mu\text{m}$ tend to be smaller than those at F444W, plausibly influenced by active starburst activity occurred at the core.

Building on the growing body of evidence, including the ubiquitous detection of $n \sim 1$ components and the strong correlation between the measured profile parameters of dust continuum and F444W, we argue that dust continuum emission originates across the disk. Furthermore, higher-resolution maps, reaching scales of down to 350 pc, reveal intricate inner structures that are bright in dust continuum. In addition to central cores and clumps, offset ridges in dust continuum are suggested in some DSFGs, indicating significance of bars.

Correlations between the dust mass surface density, stellar morphology, and core reddening (measured from rest-frame optical-to-near-infrared colors) reveal that the reddest cores are associated with the brightest and most compact dusty cores. This strongly suggests that dust extinction is the dominant factor responsible for the red colors observed in these DSFGs (see also Gillman et al. 2024). Furthermore, DSFGs with dominant red cores often exhibit Sérsic indices $n > 1$, indicating the presence of possible stellar bulges. These ob-

servations may represent an accelerated phase of bulge growth in the early universe, possibly driven by bars. The diagram also indicates the transition from immature bulges to more settled, mature stages within DSFG populations.

In the core of the $z = 3.1$ SSA22 proto-cluster, the DSFGs, associated with the cosmic web filaments, in general have a disk-like morphology. The DSFGs may assemble their mass mainly in a secular process, sustained by minor merger and gas accretion from the filaments. Notably, the most massive galaxies in the proto-cluster core tend to be late-type galaxies, presenting a striking contrast to the environmental dependence observed in the local universe. This stark difference suggests that we are witnessing the early stages of the formation of the local morphology-density relation.

This work is based on observations made with the NASA/ESA/CSA James Webb Space Telescope. The data were obtained from the Mikulski Archive for Space Telescopes at the Space Telescope Science Institute, which is operated by the Association of Universities for Research in Astronomy, Inc., under NASA contract NAS 5-03127 for JWST. These observations are associated with program #3547. This paper makes use of the following ALMA data: ADS/JAO.ALMA#2019.1.00008.S, 2021.1.00071.S. ALMA is a partnership of ESO (representing its member states), NSF (USA) and NINS (Japan), together with NRC (Canada), NSTC and ASIAA (Taiwan), and KASI (Republic of Korea), in cooperation with the Republic of Chile. The Joint ALMA Observatory is operated by ESO, AUI/NRAO and NAOJ. HU acknowledges support from JSPS KAKENHI Grant Numbers 20H01953, 22KK0231, 23K20240. This work was supported by NAOJ ALMA Scientific Research Grant Numbers 2024-26A. IRS acknowledge STFC support (ST/X001075/1).

Software: ASTROPY (Astropy Collaboration et al. 2013, 2018), CASA (CASA Team et al. 2022), CARTA (Comrie et al. 2021), GALFIT (Peng et al. 2010), LMFIT (Newville et al. 2016), MATPLOTLIB (Hunter 2007), NUMPY (Harris et al. 2020), SCIPY (Virtanen et al. 2020), SOURCE EXTRACTOR (Bertin & Arnouts 1996)

APPENDIX

Table A1. ALMA 870 μm profile measurements ($n = 1$)

ID	n	Re	b/a	P.A.
		[kpc]		[deg]
ADF22.A1	1.0	2.82 ± 0.31	0.38 ± 0.04	85.1 ± 8.6
ADF22.A3	1.0	2.21 ± 0.23	0.16 ± 0.02	75.2 ± 7.5
ADF22.A4	1.0	0.84 ± 0.08	0.89 ± 0.1	63.9 ± 13.9
ADF22.A5	1.0	2.37 ± 0.23	0.21 ± 0.02	73.2 ± 7.3
ADF22.A6	1.0	1.07 ± 0.15	0.64 ± 0.08	14.8 ± 4.1
ADF22.A7	1.0	1.30 ± 0.15	0.42 ± 0.05	18.5 ± 2.4
ADF22.A10	1.0	1.75 ± 0.23	0.29 ± 0.07	34.1 ± 4.8
ADF22.A11	1.0	1.68 ± 0.38	0.4 ± 0.13	57.9 ± 9.6

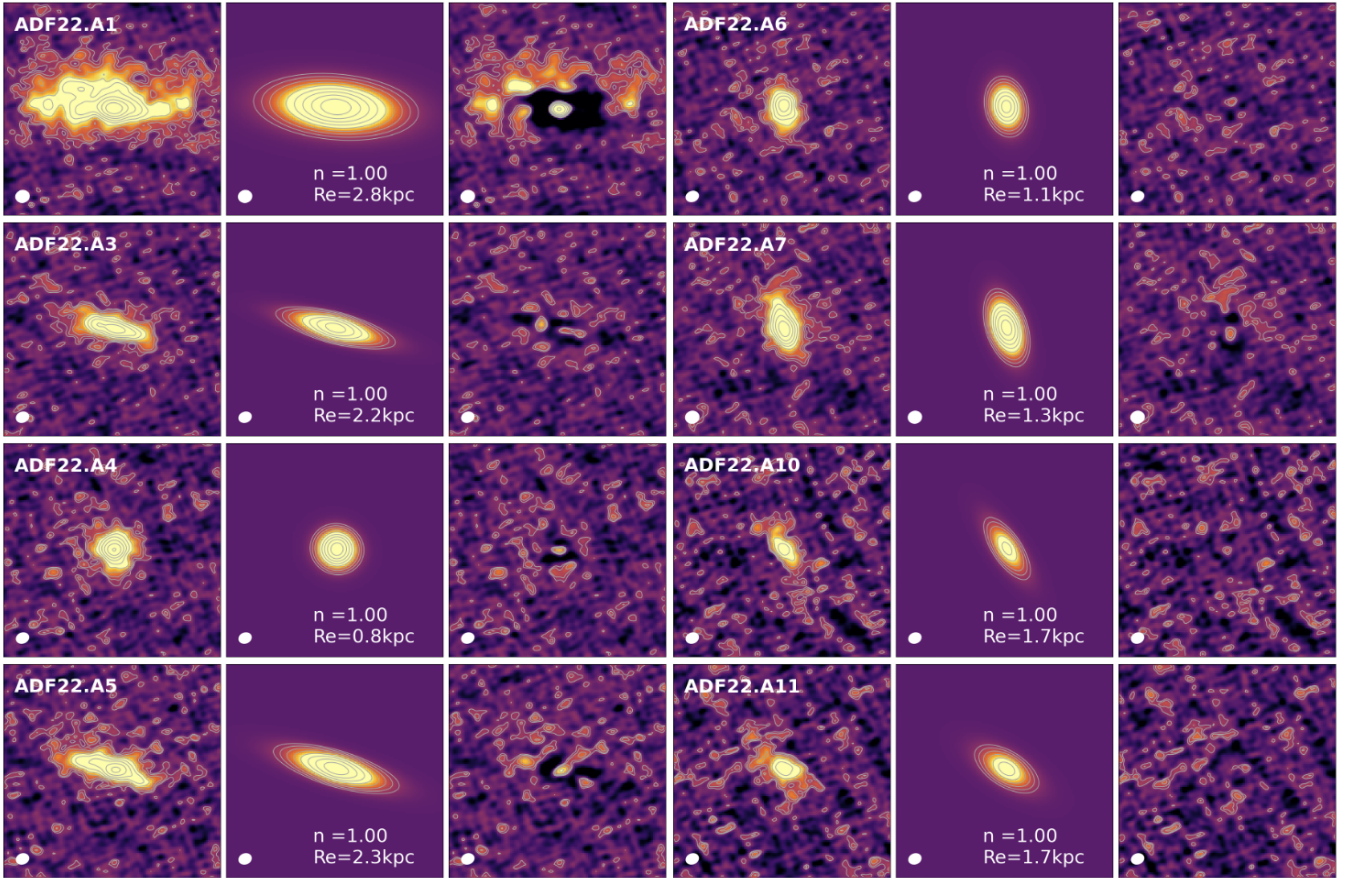


Figure A1. Results of the profile fit with ALMA 870 μm imaging on the eight brightest DSFGs in ADF22 (0.15'' resolution) in the case of fixed n ($n = 1$) without bright emission masking as Fig. 4. The fit generally causes positive and negative residuals, indicating a more complex profile for the bright DSFGs. The fits works better for the two faint DSFGs (ADF22.A10 and A11). We excluded ADF22.A16 since it is too faint for such an analysis.

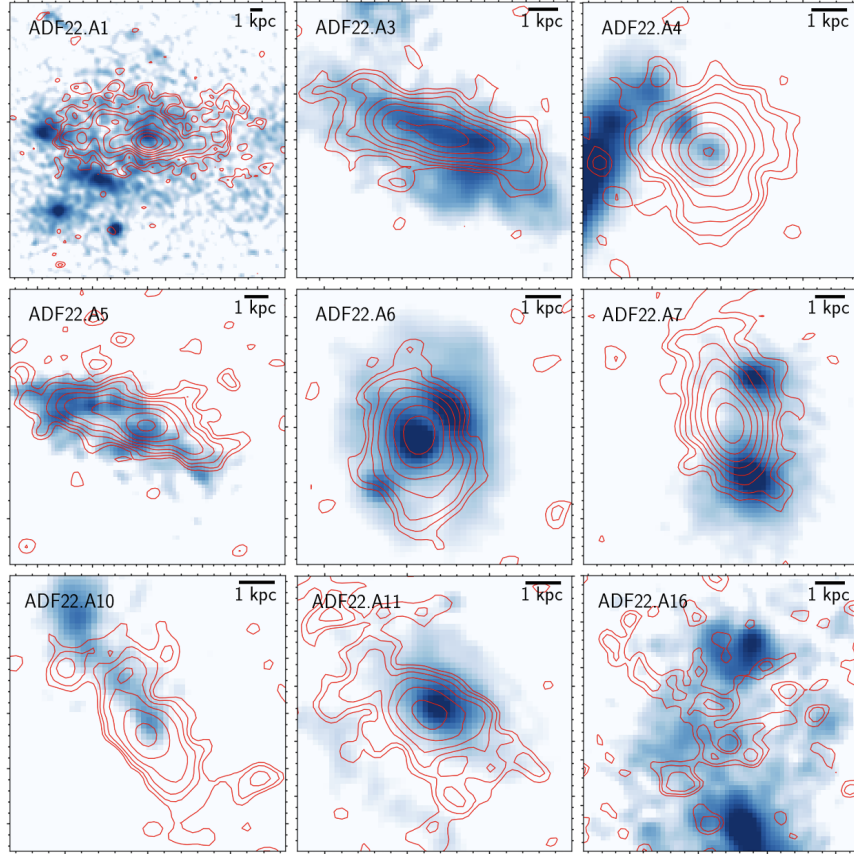


Figure B1. NIRCcam F200W images of the nine DSFGs at original spatial resolution. Contours are $\sigma \times 1.5^n$ ($n = 2 - 11$) of $870 \mu\text{m}$ emission. As shown, the relation between F200W (restframe *B*-band) emission and dust continuum emission is complex. The emission in the two bands is often segregated from each other, highlighting the significant dust obscuration at rest-frame $\approx 5000\text{\AA}$. Some of DSFGs harbor compact clumps in the F200W image. Such “blue-clumps” can be attributed by young star clusters (or AGNs).

A. RESULTS FROM THE PROFILE FIT WITH ALMA $870 \mu\text{m}$ IMAGES

B. A CLOSE UP VIEW OF ALMA AND JWST IMAGES

REFERENCES

- Amvrosiadis, A., Lange, S., Nightingale, J., et al. 2024, arXiv e-prints, arXiv:2404.01918, doi: [10.48550/arXiv.2404.01918](https://doi.org/10.48550/arXiv.2404.01918)
- Astropy Collaboration, Robitaille, T. P., Tollerud, E. J., et al. 2013, *A&A*, 558, A33, doi: [10.1051/0004-6361/201322068](https://doi.org/10.1051/0004-6361/201322068)
- Astropy Collaboration, Price-Whelan, A. M., Sipőcz, B. M., et al. 2018, *AJ*, 156, 123, doi: [10.3847/1538-3881/aabc4f](https://doi.org/10.3847/1538-3881/aabc4f)
- Bagley, M. B., Finkelstein, S. L., Koekemoer, A. M., et al. 2023, *ApJL*, 946, L12, doi: [10.3847/2041-8213/acbb08](https://doi.org/10.3847/2041-8213/acbb08)
- Barger, A. J., Cowie, L. L., Sanders, D. B., et al. 1998, *Nature*, 394, 248, doi: [10.1038/28338](https://doi.org/10.1038/28338)
- Bertin, E., & Arnouts, S. 1996, *A&AS*, 117, 393, doi: [10.1051/aas:1996164](https://doi.org/10.1051/aas:1996164)
- Blain, A. W., Chapman, S. C., Smail, I., & Ivison, R. 2004, *ApJ*, 611, 725, doi: [10.1086/422353](https://doi.org/10.1086/422353)
- Blain, A. W., Smail, I., Ivison, R. J., Kneib, J. P., & Frayer, D. T. 2002, *PhR*, 369, 111, doi: [10.1016/S0370-1573\(02\)00134-5](https://doi.org/10.1016/S0370-1573(02)00134-5)
- Bond, J. R., Kofman, L., & Pogosyan, D. 1996, *Nature*, 380, 603, doi: [10.1038/380603a0](https://doi.org/10.1038/380603a0)
- Bournaud, F., Daddi, E., Elmegreen, B. G., et al. 2008, *A&A*, 486, 741, doi: [10.1051/0004-6361:20079250](https://doi.org/10.1051/0004-6361:20079250)
- CASA Team, Bean, B., Bhatnagar, S., et al. 2022, *PASP*, 134, 114501, doi: [10.1088/1538-3873/ac9642](https://doi.org/10.1088/1538-3873/ac9642)

- Casey, C. M., Narayanan, D., & Cooray, A. 2014, *PhR*, 541, 45, doi: [10.1016/j.physrep.2014.02.009](https://doi.org/10.1016/j.physrep.2014.02.009)
- Chen, C.-C., Smail, I., Swinbank, A. M., et al. 2015, *ApJ*, 799, 194, doi: [10.1088/0004-637X/799/2/194](https://doi.org/10.1088/0004-637X/799/2/194)
- Chen, C.-C., Gao, Z.-K., Hsu, Q.-N., et al. 2022, *ApJL*, 939, L7, doi: [10.3847/2041-8213/ac98c6](https://doi.org/10.3847/2041-8213/ac98c6)
- Cheng, C., Huang, J.-S., Smail, I., et al. 2023, *ApJL*, 942, L19, doi: [10.3847/2041-8213/aca9d0](https://doi.org/10.3847/2041-8213/aca9d0)
- Colina, L., Crespo Gómez, A., Álvarez-Márquez, J., et al. 2023, *A&A*, 673, L6, doi: [10.1051/0004-6361/202346535](https://doi.org/10.1051/0004-6361/202346535)
- Comrie, A., Wang, K.-S., Hsu, S.-C., et al. 2021, *CARTA: The Cube Analysis and Rendering Tool for Astronomy*, 2.0.0, Zenodo, doi: [10.5281/zenodo.4905459](https://doi.org/10.5281/zenodo.4905459)
- Conselice, C. J., Grogin, N. A., Jogee, S., et al. 2004, *ApJL*, 600, L139, doi: [10.1086/378556](https://doi.org/10.1086/378556)
- da Cunha, E., Groves, B., Walter, F., et al. 2013, *ApJ*, 766, 13, doi: [10.1088/0004-637X/766/1/13](https://doi.org/10.1088/0004-637X/766/1/13)
- Daddi, E., Dannerbauer, H., Stern, D., et al. 2009, *ApJ*, 694, 1517, doi: [10.1088/0004-637X/694/2/1517](https://doi.org/10.1088/0004-637X/694/2/1517)
- De Lucia, G., Springel, V., White, S. D. M., Croton, D., & Kauffmann, G. 2006, *MNRAS*, 366, 499, doi: [10.1111/j.1365-2966.2005.09879.x](https://doi.org/10.1111/j.1365-2966.2005.09879.x)
- de Vaucouleurs, G. 1948, *Annales d'Astrophysique*, 11, 247
- Dekel, A., & Birnboim, Y. 2006, *MNRAS*, 368, 2, doi: [10.1111/j.1365-2966.2006.10145.x](https://doi.org/10.1111/j.1365-2966.2006.10145.x)
- Dekel, A., Birnboim, Y., Engel, G., et al. 2009, *Nature*, 457, 451, doi: [10.1038/nature07648](https://doi.org/10.1038/nature07648)
- Dressler, A. 1980, *ApJ*, 236, 351, doi: [10.1086/157753](https://doi.org/10.1086/157753)
- Dunlop, J. S., McLure, R. J., Biggs, A. D., et al. 2017, *MNRAS*, 466, 861, doi: [10.1093/mnras/stw3088](https://doi.org/10.1093/mnras/stw3088)
- Eales, S., Lilly, S., Gear, W., et al. 1999, *ApJ*, 515, 518, doi: [10.1086/307069](https://doi.org/10.1086/307069)
- Ellis, R. S., Smail, I., Dressler, A., et al. 1997, *ApJ*, 483, 582, doi: [10.1086/304261](https://doi.org/10.1086/304261)
- Elmegreen, B. G., & Elmegreen, D. M. 2005, *ApJ*, 627, 632, doi: [10.1086/430514](https://doi.org/10.1086/430514)
- Elmegreen, B. G., Elmegreen, D. M., Fernandez, M. X., & Lemonias, J. J. 2009, *ApJ*, 692, 12, doi: [10.1088/0004-637X/692/1/12](https://doi.org/10.1088/0004-637X/692/1/12)
- Elmegreen, D. M., Elmegreen, B. G., Ravindranath, S., & Coe, D. A. 2007, *ApJ*, 658, 763, doi: [10.1086/511667](https://doi.org/10.1086/511667)
- Genzel, R., Burkert, A., Bouché, N., et al. 2008, *ApJ*, 687, 59, doi: [10.1086/591840](https://doi.org/10.1086/591840)
- Genzel, R., Newman, S., Jones, T., et al. 2011, *ApJ*, 733, 101, doi: [10.1088/0004-637X/733/2/101](https://doi.org/10.1088/0004-637X/733/2/101)
- Gillman, S., Gullberg, B., Brammer, G., et al. 2023, *A&A*, 676, A26, doi: [10.1051/0004-6361/202346531](https://doi.org/10.1051/0004-6361/202346531)
- Gillman, S., Smail, I., Gullberg, B., et al. 2024, *A&A*, 691, A299, doi: [10.1051/0004-6361/202451006](https://doi.org/10.1051/0004-6361/202451006)
- Greve, T. R., Bertoldi, F., Smail, I., et al. 2005, *MNRAS*, 359, 1165, doi: [10.1111/j.1365-2966.2005.08979.x](https://doi.org/10.1111/j.1365-2966.2005.08979.x)
- Gullberg, B., Swinbank, A. M., Smail, I., et al. 2018, *ApJ*, 859, 12, doi: [10.3847/1538-4357/aabe8c](https://doi.org/10.3847/1538-4357/aabe8c)
- Gullberg, B., Smail, I., Swinbank, A. M., et al. 2019, *MNRAS*, 490, 4956, doi: [10.1093/mnras/stz2835](https://doi.org/10.1093/mnras/stz2835)
- Hainline, L. J., Blain, A. W., Smail, I., et al. 2011, *ApJ*, 740, 96, doi: [10.1088/0004-637X/740/2/96](https://doi.org/10.1088/0004-637X/740/2/96)
- Harris, C. R., Millman, K. J., van der Walt, S. J., et al. 2020, *Nature*, 585, 357, doi: [10.1038/s41586-020-2649-2](https://doi.org/10.1038/s41586-020-2649-2)
- Hayashino, T., Matsuda, Y., Tamura, H., et al. 2004, *AJ*, 128, 2073, doi: [10.1086/424935](https://doi.org/10.1086/424935)
- Hayatsu, N. H., Matsuda, Y., Umehata, H., et al. 2017, *PASJ*, 69, 45, doi: [10.1093/pasj/psx018](https://doi.org/10.1093/pasj/psx018)
- Hodge, J. A., & da Cunha, E. 2020, *Royal Society Open Science*, 7, 200556, doi: [10.1098/rsos.200556](https://doi.org/10.1098/rsos.200556)
- Hodge, J. A., Karim, A., Smail, I., et al. 2013, *ApJ*, 768, 91, doi: [10.1088/0004-637X/768/1/91](https://doi.org/10.1088/0004-637X/768/1/91)
- Hodge, J. A., Swinbank, A. M., Simpson, J. M., et al. 2016, *ApJ*, 833, 103, doi: [10.3847/1538-4357/833/1/103](https://doi.org/10.3847/1538-4357/833/1/103)
- Hodge, J. A., Smail, I., Walter, F., et al. 2019, *ApJ*, 876, 130, doi: [10.3847/1538-4357/ab1846](https://doi.org/10.3847/1538-4357/ab1846)
- Hodge, J. A., Cunha, E. d., Kendrew, S., et al. 2025, *ApJ*, 978, 165, doi: [10.3847/1538-4357/ad9a52](https://doi.org/10.3847/1538-4357/ad9a52)
- Hopkins, P. F., Hernquist, L., Cox, T. J., et al. 2006, *ApJS*, 163, 1, doi: [10.1086/499298](https://doi.org/10.1086/499298)
- Hughes, D. H., Serjeant, S., Dunlop, J., et al. 1998, *Nature*, 394, 241, doi: [10.1038/28328](https://doi.org/10.1038/28328)
- Hunter, J. D. 2007, *Computing in Science and Engineering*, 9, 90, doi: [10.1109/MCSE.2007.55](https://doi.org/10.1109/MCSE.2007.55)
- Ikarashi, S., Ivison, R. J., Cowley, W. I., & Kohno, K. 2022, *A&A*, 659, A154, doi: [10.1051/0004-6361/202141196](https://doi.org/10.1051/0004-6361/202141196)
- Ikarashi, S., Ivison, R. J., Caputi, K. I., et al. 2015, *ApJ*, 810, 133, doi: [10.1088/0004-637X/810/2/133](https://doi.org/10.1088/0004-637X/810/2/133)
- Iono, D., Yun, M. S., Aretxaga, I., et al. 2016, *ApJL*, 829, L10, doi: [10.3847/2041-8205/829/1/L10](https://doi.org/10.3847/2041-8205/829/1/L10)
- Ivison, R. J., Smail, I., Le Borgne, J. F., et al. 1998, *MNRAS*, 298, 583, doi: [10.1046/j.1365-8711.1998.01677.x](https://doi.org/10.1046/j.1365-8711.1998.01677.x)
- Kodama, T., Arimoto, N., Barger, A. J., & Arag'ón-Salamanca, A. 1998, *A&A*, 334, 99, doi: [10.48550/arXiv.astro-ph/9802245](https://doi.org/10.48550/arXiv.astro-ph/9802245)
- Kodama, T., Tanaka, I., Kajisawa, M., et al. 2007, *MNRAS*, 377, 1717, doi: [10.1111/j.1365-2966.2007.11739.x](https://doi.org/10.1111/j.1365-2966.2007.11739.x)
- Kruk, S. J., Lintott, C. J., Bamford, S. P., et al. 2018, *MNRAS*, 473, 4731, doi: [10.1093/mnras/stx2605](https://doi.org/10.1093/mnras/stx2605)
- Kubo, M., Yamada, T., Ichikawa, T., et al. 2016, *MNRAS*, 455, 3333, doi: [10.1093/mnras/stv2392](https://doi.org/10.1093/mnras/stv2392)
- Lemson, G., & Kauffmann, G. 1999, *MNRAS*, 302, 111, doi: [10.1046/j.1365-8711.1999.02090.x](https://doi.org/10.1046/j.1365-8711.1999.02090.x)

- Li, A., & Draine, B. T. 2001, *ApJ*, 554, 778, doi: [10.1086/323147](https://doi.org/10.1086/323147)
- Matsuda, Y., Yamada, T., Hayashino, T., et al. 2005, *ApJL*, 634, L125, doi: [10.1086/499071](https://doi.org/10.1086/499071)
- Miller, T. B., Chapman, S. C., Aravena, M., et al. 2018, *Nature*, 556, 469, doi: [10.1038/s41586-018-0025-2](https://doi.org/10.1038/s41586-018-0025-2)
- Monson, E. B., Lehmer, B. D., Doore, K., et al. 2021, *ApJ*, 919, 51, doi: [10.3847/1538-4357/ac0f84](https://doi.org/10.3847/1538-4357/ac0f84)
- Monson, E. B., Doore, K., Eufrazio, R. T., et al. 2023, *ApJ*, 951, 15, doi: [10.3847/1538-4357/acd449](https://doi.org/10.3847/1538-4357/acd449)
- Newville, M., Stensitzki, T., Allen, D. B., et al. 2016, *Lmfit: Non-Linear Least-Square Minimization and Curve-Fitting for Python*, Astrophysics Source Code Library, record ascl:1606.014
- Oteo, I., Ivison, R. J., Dunne, L., et al. 2018, *ApJ*, 856, 72, doi: [10.3847/1538-4357/aaalf1](https://doi.org/10.3847/1538-4357/aaalf1)
- Peng, C. Y., Ho, L. C., Impey, C. D., & Rix, H.-W. 2002, *AJ*, 124, 266, doi: [10.1086/340952](https://doi.org/10.1086/340952)
- . 2010, *AJ*, 139, 2097, doi: [10.1088/0004-6256/139/6/2097](https://doi.org/10.1088/0004-6256/139/6/2097)
- Perrin, M. D., Sivaramakrishnan, A., Lajoie, C.-P., et al. 2014, in *Society of Photo-Optical Instrumentation Engineers (SPIE) Conference Series*, Vol. 9143, *Space Telescopes and Instrumentation 2014: Optical, Infrared, and Millimeter Wave*, ed. J. Oschmann, Jacobus M., M. Clampin, G. G. Fazio, & H. A. MacEwen, 91433X, doi: [10.1117/12.2056689](https://doi.org/10.1117/12.2056689)
- Popping, G., Pillepich, A., Calistro Rivera, G., et al. 2022, *MNRAS*, 510, 3321, doi: [10.1093/mnras/stab3312](https://doi.org/10.1093/mnras/stab3312)
- Riechers, D. A., Bradford, C. M., Clements, D. L., et al. 2013, *Nature*, 496, 329, doi: [10.1038/nature12050](https://doi.org/10.1038/nature12050)
- Rizzo, F., Roman-Oliveira, F., Fraternali, F., et al. 2023, *A&A*, 679, A129, doi: [10.1051/0004-6361/202346444](https://doi.org/10.1051/0004-6361/202346444)
- Scoville, N., Sheth, K., Aussel, H., et al. 2016, *ApJ*, 820, 83, doi: [10.3847/0004-637X/820/2/83](https://doi.org/10.3847/0004-637X/820/2/83)
- Sersic, J. L. 1968, *Atlas de Galaxias Australes*
- Simpson, J. M., Swinbank, A. M., Smail, I., et al. 2014, *ApJ*, 788, 125, doi: [10.1088/0004-637X/788/2/125](https://doi.org/10.1088/0004-637X/788/2/125)
- Simpson, J. M., Smail, I., Swinbank, A. M., et al. 2015, *ApJ*, 799, 81, doi: [10.1088/0004-637X/799/1/81](https://doi.org/10.1088/0004-637X/799/1/81)
- . 2017, *ApJ*, 839, 58, doi: [10.3847/1538-4357/aa65d0](https://doi.org/10.3847/1538-4357/aa65d0)
- Smail, I., Ivison, R. J., & Blain, A. W. 1997, *ApJL*, 490, L5, doi: [10.1086/3111017](https://doi.org/10.1086/3111017)
- Smail, I., Dudzevičiūtė, U., Stach, S. M., et al. 2021, *MNRAS*, 502, 3426, doi: [10.1093/mnras/stab283](https://doi.org/10.1093/mnras/stab283)
- Smail, I., Dudzevičiūtė, U., Gurwell, M., et al. 2023, *ApJ*, 958, 36, doi: [10.3847/1538-4357/acf931](https://doi.org/10.3847/1538-4357/acf931)
- Smith, R. J., Lucey, J. R., & Carter, D. 2012, *MNRAS*, 426, 2994, doi: [10.1111/j.1365-2966.2012.21922.x](https://doi.org/10.1111/j.1365-2966.2012.21922.x)
- Springel, V., White, S. D. M., Jenkins, A., et al. 2005, *Nature*, 435, 629, doi: [10.1038/nature03597](https://doi.org/10.1038/nature03597)
- Stach, S. M., Dudzevičiūtė, U., Smail, I., et al. 2019, *MNRAS*, 487, 4648, doi: [10.1093/mnras/stz1536](https://doi.org/10.1093/mnras/stz1536)
- Steidel, C. C., Adelberger, K. L., Dickinson, M., et al. 1998, *ApJ*, 492, 428, doi: [10.1086/305073](https://doi.org/10.1086/305073)
- Stevens, J. A., Ivison, R. J., Dunlop, J. S., et al. 2003, *Nature*, 425, 264, doi: [10.1038/nature01976](https://doi.org/10.1038/nature01976)
- Sun, F., Helton, J. M., Egami, E., et al. 2024, *ApJ*, 961, 69, doi: [10.3847/1538-4357/ad07e3](https://doi.org/10.3847/1538-4357/ad07e3)
- Swinbank, A. M., Smail, I., Chapman, S. C., et al. 2010, *MNRAS*, 405, 234, doi: [10.1111/j.1365-2966.2010.16485.x](https://doi.org/10.1111/j.1365-2966.2010.16485.x)
- Tadaki, K., Iono, D., Yun, M. S., et al. 2018, *Nature*, 560, 613, doi: [10.1038/s41586-018-0443-1](https://doi.org/10.1038/s41586-018-0443-1)
- Tamura, Y., Kohno, K., Nakanishi, K., et al. 2009, *Nature*, 459, 61, doi: [10.1038/nature07947](https://doi.org/10.1038/nature07947)
- Tamura, Y., Iono, D., Wilner, D. J., et al. 2010, *ApJ*, 724, 1270, doi: [10.1088/0004-637X/724/2/1270](https://doi.org/10.1088/0004-637X/724/2/1270)
- Tan, Q.-H., Daddi, E., Magnelli, B., et al. 2024, *Nature*, 636, 69, doi: [10.1038/s41586-024-08201-6](https://doi.org/10.1038/s41586-024-08201-6)
- Toft, S., Smolčić, V., Magnelli, B., et al. 2014, *ApJ*, 782, 68, doi: [10.1088/0004-637X/782/2/68](https://doi.org/10.1088/0004-637X/782/2/68)
- Tsukui, T., Wisnioski, E., Bland-Hawthorn, J., et al. 2024, *MNRAS*, 527, 8941, doi: [10.1093/mnras/stad3588](https://doi.org/10.1093/mnras/stad3588)
- Umehata, H., Tamura, Y., Kohno, K., et al. 2014, *MNRAS*, 440, 3462, doi: [10.1093/mnras/stu447](https://doi.org/10.1093/mnras/stu447)
- . 2015, *ApJL*, 815, L8, doi: [10.1088/2041-8205/815/1/L8](https://doi.org/10.1088/2041-8205/815/1/L8)
- . 2017, *ApJ*, 835, 98, doi: [10.3847/1538-4357/835/1/98](https://doi.org/10.3847/1538-4357/835/1/98)
- Umehata, H., Hatsukade, B., Smail, I., et al. 2018, *PASJ*, 70, 65, doi: [10.1093/pasj/psy065](https://doi.org/10.1093/pasj/psy065)
- Umehata, H., Fumagalli, M., Smail, I., et al. 2019, *Science*, 366, 97, doi: [10.1126/science.aaw5949](https://doi.org/10.1126/science.aaw5949)
- Umehata, H., Smail, I., Swinbank, A. M., et al. 2020, *A&A*, 640, L8, doi: [10.1051/0004-6361/202038146](https://doi.org/10.1051/0004-6361/202038146)
- Umehata, H., Steidel, C. C., Smail, I., et al. 2024, *arXiv e-prints*, arXiv:2410.22155, doi: [10.48550/arXiv.2410.22155](https://doi.org/10.48550/arXiv.2410.22155)
- Virtanen, P., Gommers, R., Oliphant, T. E., et al. 2020, *Nature Methods*, 17, 261, doi: [10.1038/s41592-019-0686-2](https://doi.org/10.1038/s41592-019-0686-2)
- Walter, F., Decarli, R., Carilli, C., et al. 2012, *Nature*, 486, 233, doi: [10.1038/nature11073](https://doi.org/10.1038/nature11073)
- Wardlow, J. L., Smail, I., Coppin, K. E. K., et al. 2011, *MNRAS*, 415, 1479, doi: [10.1111/j.1365-2966.2011.18795.x](https://doi.org/10.1111/j.1365-2966.2011.18795.x)
- Weiß, A., De Breuck, C., Marrone, D. P., et al. 2013, *ApJ*, 767, 88, doi: [10.1088/0004-637X/767/1/88](https://doi.org/10.1088/0004-637X/767/1/88)